# TELESCOPE SCIENTIST ON THE ADVANCED X-RAY ASTROPHYSICS OBSERVATORY

The article appended here and published in the *AXAF News* summarizes the work completed on this project during the referenced period.

IN-10
[illegible]

NASA Grant NAG8-792

FINAL Report

For the Period 13 January 1990 through 12 January 1999

Principal Investigator
Dr. Leon Van Speybroeck

Prepared for:

National Aeronautics and Space Administration
George C. Marshall Space Flight Center
Marshall Space Flight Center, Alabama 35812

Smithsonian Institution
Astrophysical Observatory
Cambridge, Massachusetts 02138

The Smithsonian Astrophysical Observatory
is a member of the
Harvard-Smithsonian Center for Astrophysics

The NASA Technical Officer for this grant is Dr. Max E. Rosenthal, NASA, George C. Marshall Space Flight Center, Code TA61, Marshall Space Flight Center, Alabama 35812.

NASA Grant NAG8-792
AXAF Telescope Scientist
Period of Performance: 13 January, 1997 to 12 January, 1998.

## 1. Introduction.

The most important activity during this reporting period was the calibration of the AXAF High Resolution Mirror Assembly (HRMA) and the analysis of the copious data which were obtained during that project. The calibration was highly successful, and will result in the AXAF being by far the best calibrated X-ray observatory ever flown, and more accurate results by all of its users. This period also included participation in the spacecraft alignment and assembly activities and final flight readiness reviews. The planning of the first year of Telescope Scientist AXAF observations also was accomplished. The Telescope Scientist team also served as a technical resource for various problems which were encountered during this period. Many of these contributions have been documented in memoranda sent to the project.

## 2. AXAF Mirror Calibration.

The test activity was a team effort with critical contributions from many organizations, including MSFC, SAO, the science instrument groups, and TRW and their sub-contractors. The Telescope Scientist Team contributed to the planning of the test program. The Telescope Scientist served as a member of the Project Science Team which was led by Dr. Martin Weisskopf and was responsible for the actual performance of the tests, including deviations from the test plan necessitated by equipment malfunctions or unexpected experimental results. As stated above, the final calibration was remarkably successful.

The analysis of these data has been led by the AXAF Mission Support Team under the direction of Dr. Daniel Schwartz, but with important contributions from the MSFC science team and from the Telescope Scientist Team. The latter group has contributed scientific guidance to the project and been responsible for many details of the analysis.

The Telescope Scientist Team calculated the expected scattering distributions which resulted from high frequency mirror surface errors; these calculations were used to model the observed image distributions and to correct effective area measurements for wide angle scattering losses. The analysis is adequate at the $\sim$ 5% level, but must the theory must be improved to achieve the objective $\sim$ 1% level. We have begun work upon improvements to the theory which will treat the surface interactions more accurately.

The Telescope Scientist Team analyzed the XRCF HRMA effective area data measured with a carbon-continuum source and solid state detectors. Effects such as the SSD response, pileup correction, energy scale, deadtime correction, quantum efficiency, background, icing effect, *etc.* were evaluated carefully. The measured effective area for each mirror shell was determined as a function of energy. The results show that the measured effective area is less than the raytrace predicted effective area by 5–10% at energies approaching the reflection cutoff energy, which is more than the experimental errors. The most probable cause of this discrepancy is due to inadequacies in the surface reflection efficiency modeling, which are currently being investigated. The current models are based upon measurements of very smooth flats and treat the surface roughness as a small perturbation without low frequency errors. The Telescope Scientist Team is developing improved reflection models which include lower frequency errors and the effects of a finite surface density gradient.

The detailed analysis contributions by the Telescope Scientist Team included careful consideration of the HRMA X-ray Detection System (especially the window and mesh corrections), spectral line data consistency, wing scan data corrections, X-ray scattering from different surface roughness models to investigate the possible extra losses of the HRMA effective area, studies of synchrotron mirror reflectivity data and analysis, the HRMA ring focus shutter test, and HRMA ring focus measurements. Many of these contributions were included in the HRMA calibration report to NASA.

The Telescope Scientist Team used the calibration data to scale down the raytrace empirically for both on-orbit and XRCF HRMA effective area predictions. The C-continuum SSD data were used for E>2 keV and spectral line FPC data for E<2 keV to calibrate the HRMA effective area. Web pages were generated to distribute the calibrated HRMA effective area (both figures and rdb tables). This work serves the AXAF community for making the AXAF on-orbit performance predictions, and for other AXAF teams to calibrate their science instruments. This work was presented at the SPIE conference and written as a report to NASA. The AXAF on orbit performance predictions were used in the material provided to the scientific community with the the release of NASA AXAF AO-1. These effective area and image distribution predictions were used as part of the AXAF Science Center (ASC) documents "AXAF Observatory Guide" and "AXAF Proposers' Guide", and will be used with tools in the DETECT pipeline for the actual AXAF data reduction. Supplementary support also was provided to proposers other members of the AXAF community. The SPIE paper is included as Appendix A.

**3.** Miscellaneous Program Support.

The Telescope Scientist Team provided support on a number of technical problems which were encountered during this phase of the program. Some of these included support to the alignment activities, support to the aspect camera calibration, advice on stray light requirements, consideration of ice formation as a possible explanation of the ACIS door failure during thermal vacuum testing, and service upon the AXAF Flight Readiness Review Board.

**4.** Science Program.

The Telescope Scientist guaranteed time observations will be devoted to observations of distant galaxy clusters to study their evolution and to determine cosmological scale quantities using the Sunyaev Zel'dovich effect. Cooperative agreements with other scientists, including radio observers, have been formed and the first year's observation targets have been selected.

This list has been used by radio observers to guide their selection of clusters to be studied. Some systematic effects of projection effects also have been made; these studies show that a sample of order 20 clusters is required to reduce the projection effects to the desired fraction of the total error budget. A memorandum summarizing these effects is included as Appendix B.

Dr. Ping Zhao of the Telescope Scientist Team continued his research in the area of black-hole binary systems and classical and X-ray novae. He performed observations using the Telescopes on Mt. Hopkins, and presented his research results in two AAS meetings.

# Appendix A

# AXAF Mirror Effective Area Calibration Using the C-continuum Source and Solid State Detectors.

SAO-AXAF-DR-98-344
Rev "A"
September 1998
Data Type: 3

Advanced X-Ray Astrophysics Facility (AXAF)

Mission Support

NAS8-40224

# AXAF Mirror Effective Area Calibration Using the C-continuum Source and Solid State Detectors

September 1998

Prepared in accordance with DRD# 784MA-002

Principal Investigator

Dr. H. D. Tananbaum

Prepared for:
George C. Marshall Space Flight Center
National Aeronautics and Space Administration
Marshall Space Flight Center, AL 35812

Smithsonian Astrophysical Observatory
60 Garden Street
Cambridge, MA 02138

Smithsonian Institution
Astrophysical Observatory

**Title:** AXAF Mirror Effective Area Calibration Using the C-continuum Source and Solid State Detectors

**Date:** September 1998

**Document No.:** SAO-AXAF-DR-98-344

**DRD No.:** 784MA-002

**Prepared by:** P.Zhao

**Data Type:** 3

**Filename:** (wp51; c:MA-002.344)

**APPROVAL SIGNATURES**

Ping Zhao 9/21/98
Science Date

Francis E. Cocuzzo 9/23/98
Deputy Program Manager Date

# AXAF Mirror Effective Area Calibration Using the C-continuum Source and Solid State Detectors

Ping Zhao,[a1] R. A. Austin,[c] R. J. Edgar,[a] R. F. Elsner,[b] T. J. Gaetz,[a],
D. E. Graessle,[a] D. Jerius,[a] J. J. Kolodziejczak,[c] W. C. McDermott,[a]
S. L. O'Dell,[b] M. E. Sulkanen,[b] D. A. Schwartz,[a] D. A. Swartz,[c] A. F. Tennant,[b]
L. P. Van Speybroeck,[a] B. J. Wargelin,[a] M. C. Weisskopf,[b] C. G. Zirnstein[c]

[a]Smithsonian Astrophysical Observatory, 60 Garden Street, Cambridge, MA 02138 U.S.A.
[b]NASA, Space Science Laboratory, Marshall Space Flight Center, Huntsville, AL 35812, U.S.A.
[c]USRA, Space Science Laboratory, Marshall Space Flight Center, Huntsville, AL 35812, U.S.A.

## ABSTRACT

The Advanced X-ray Astrophysics Facility (AXAF) X-ray mirrors underwent thorough calibration using the X-Ray Calibration Facility (XRCF) at the Marshall Space Flight Center (MSFC) in Huntsville, AL from late 1996 to early 1997. The X-ray calibration made novel use of the X-ray continuum from a conventional electron-impact source. Taking advantage of the good spectral resolution of solid-state detectors, continuum measurements proved advantageous in calibrating the effective area of AXAF's High-Resolution Mirror Assembly (HRMA) for the entire AXAF energy band. The measurements were made by comparing the spectrum detected by a SSD at the focal plane with the spectrum detected by a beam normalization SSD. The HRMA effective area was calibrated by comparing the measurements with the HRMA raytrace model. The HRMA on-orbit performance predictions are made using the calibration results.

**Keywords:** AXAF, HRMA, X-ray mirror, X-ray sources, calibration, effective area, solid state detector, raytrace.

## 1 INTRODUCTION

The launch of the most powerful X-ray telescope ever built – NASA's Advanced X-ray Astrophysics Facility (AXAF) – is a major milestone in high energy astrophysics and the world of science. It will serve as an important astrophysical research facility to bridge into the 21st Century. AXAF is the X-ray component of NASA's Great Observatories. It represents the most advanced science and technology in the world today. It will follow Hubble Space Telescope and Compton Gamma Ray Observatory's success to open a new window to the Universe. AXAF has unprecedented capabilities of high resolution imaging and spectroscopy over the X-ray band of 0.1 keV – 10 keV.

To ensure a successful scientific mission, an extensive ground calibration for the AXAF mirror and science instruments was carried out at NASA's Marshall Space Flight Center from September 1996 through May 1997. It was determined that the AXAF effective area should be calibrated to a precision that no X-ray telescopes have ever achieved before – 1%. This will enable AXAF to provide unprecedented precision to measure the flux from X-ray sources.

During the calibration, the HRMA on-axis effective area was measured in two different ways in terms of the X-ray source characteristics: the discrete line measurements and the carbon-continuum (C-continuum) measurements. The former uses characteristic X-ray lines generated by an Electron Impact Point Source (EIPS) with various anodes. The latter uses continuum X-ray radiation generated by EIPS with a carbon anode at 15 kV and using a beryllium (Be) filter to attenuate the lowest energies including the C-K$\alpha$ line (0.277 keV). A preliminary result of this measurement was reported in SPIE '98. [1]

For the X-ray line measurements, both Flow Proportional Counter (FPC) and Solid State Detector (SSD) were used. For the FPC, 4 energy lines were used for four individual shells effective area measurements, and 3 energy lines were used for the HRMA (all four shells open) effective area measurements. Several other energy lines were used for the HRMA or MEG (Shells 1 and 3 open) or HEG (Shells 4 and 6 open) configurations and with 1 mm and

---

[1] Further author information – Ping Zhao (correspondence): Email: zhao@cfa.harvard.edu; Phone: 617-496-7582; Fax: 617-495-7356

**Table 1: HRMA On-axis Effective Area Measurenents**
Source: C-continuum Detector: SSD

| TRW ID | Run ID | Date | Shell | Aper ($\mu$m) | Int (sec) |
|---|---|---|---|---|---|
| E-IXS-MC-15.001 | 110539 | 970130 | 1 | 2000 | 1000 |
| E-IXS-MC-15.002 | 110540 | 970130 | 3 | 2000 | 1000 |
| E-IXS-MC-15.003 | 110541 | 970130 | 4 | 2000 | 1000 |
| E-IXS-MC-15.004 | 110542 | 970130 | 6 | 2000 | 1000 |

0.5 mm apertures only. For the SSD, 3 energy lines were used for the HRMA. Four energy lines were used for the MEG and HEG configurations and with 0.5 mm aperture only. No SSD measurements were made for the effective area of individual shells.

For the continuum measurements, only SSD was used, and only the effective area of each individual shell were measured. The effective area was measured for each individual mirror shell by comparing the spectrum detected by SSX (SSD at the HRMA focal plane) with the spectrum detected simultaneously by SS5 (SSD in Building 500 of the XRCF, to one side of the X-ray beam). The continuum measurements have the advantage of providing the effective area data for nearly the entire AXAF energy band, but the data analysis and results evaluation need careful attention. Factors such as SSD response, pileup correction, energy scale, deadtime correction, quantum efficiency, background, icing effect, *etc.*, need to be carefully evaluated.

This paper discusses the data analysis and HRMA effective area measured using the C-continuum source and solid state detectors. The results are compared with the X-ray line measurements and with the HRMA raytracing models. The comparison are used to make an on-orbit HRMA effective area prediction.

## 2 SSD C-CONTINUUM EFFECTIVE AREA MEASUREMENTS

The effective area measurements with the C-continuum Source were made with two nearly identical high-purity-germanium solid state detectors: one (SS5) is a beam-normalization-detector (BND) located at 38.199 meters from the source in Building 500 of the XRCF, another one (SSX) is the focal plane detector located at the HRMA focus, 537.778 meters from the source. An aperture wheel was mounted in front of each SSD. The HRMA effective area was measured with a 2 mm diameter aperture in front of the SS5 and apertures with various sizes in front of the SSX.

The on-axis effective area measurements with the C-continuum source and SSD detectors were made on 970113 (Date notation for 13 Jan 1997) with various apertures on SSX and 300-second integrations, and on 970130 with only the 2 mm aperture on SSX and 1000-second integrations. The off-axis effective area measurements with C-continuum were also made on 970131 with various apertures on SSX, 300-second integrations, and off-axis angles of 5′, 10′, 15′, 20′, 25′, and 30′.

This paper focuses on the on-axis effective area measurements made on 970130. They have the TRW IDs E-IXS-MC-15.001,2,3,4 (Run ID: 110539, 110540, 110541, 110542) and the longest integration time and the largest apertures used for this kind of measurement. We use this set of data to demonstrate the data reduction and to make the HRMA effective area predictions. All other sets of data can be processed the same way. Table 1 lists this set of measurements. Figure 1 shows the SSX and SS5 spectra of these four measurements. The profiles show the C-continuum spectra with several spectral peaks on top. The largest Gaussian-like peak at around channels 2400–2500 is the injected pulser spectrum to be used for the pileup and deadtime corrections (see §3 and §6). Other peaks are characteristic X-ray lines due to contaminations to the carbon anode. These peaks will be used to determine the energy scale (see §5).

## 3 PILEUP CORRECTION

Before analyzing the SSD spectra, the first thing to do is to make the pileup correction. Pileups are when more than one photon enter the detector within a small time window (a few $\mu$sec). Instead of recording each photon event, the detector registers only one event with the summed energy of all photons. The pileup can also occur for a real photon with a pulser event. The SSD has pileup rejection electronics to reduce the pileup. However, the rejection does not work well if one of the photons has energy below 2 keV, corresponding to a pre-amplifier output signal of 4 mV. Thus each spectrum needs to be corrected for pileups of any photon with a low energy ($< 2$ keV) photon. Since three or more photon pileups are extremely rare events and their effect is negligible, we only consider two photon pileups.

We use the SSD pulser spectra to establish an empirical pileup model. As shown in the SSX pulser spectra for shell 1 and 3 (see Figure 1), the pulser pileups are clearly shown to the right of the pulser peak. In the SSX pulser spectra for shell 4 and 6, the pulser pileups are mixed with the continuum pileups to the right of the pulser peak. In the SS5 pulser spectra, the continuum dominates the right side of the pulser peak; the pileup effects are very small since they are proportional to the counting rate. The total continuum counting rates in SS5 are 1–2 orders of magnitude lower than that of SSX. Therefore we use the SSX pulser spectra for shell 1 and 3, where the pulser pileup effects are clear and not mixed with the continuum pileups, to establish the model for the pileup correction. We first divide the pulser pileup region into four bands with 100 channels per band. Since 2 keV $\approx$ 400 channels, counts in these regions are pileups of low energy photons ($< 2$ keV) with the pulser. Since the pileups are proportional to counting rate of photons $< 2$ keV, we define a pileup rate as the pulser pileup fraction (pulser pileup counts divided by the total pulser counts) divided by the counting rate within channels 0–400. Both SSX spectra give, as it should be, about the same results: for the four 100-channel windows after the pulser, the pileup rates are $1.2\times10^{-6}$ sec/count in channels 1-100, $1.0\times10^{-6}$ sec/count in channels 101–200, $0.7\times10^{-6}$ sec/count in channels 201–300, and $0.3\times10^{-6}$ sec/count in channels 301-400. Notice that here the unit for pileup rate is "second/count". When calculating the pileup fraction, we need to multiply these pileup rates by the counting rate within channels 0–400. For example, for SSX spectrum 110539, CR(0–400) = 4448 counts/second, pileup fractions are 0.005337, 0.004448, 0.003114, 0.001334 in the four windows; for SSX spectrum 110542, CR(0–400) = 1415 counts/second, pileup fractions are 0.001698, 0.001415, 0.000990, 0.000424. Meantime, for all the SS5 spectra, CR(0–400) = 100, so the pileup fractions are 0.000120, 0.000100, 0.000070, 0.000030, which are negligible.

In each channel of the raw spectra, there are real events at that energy plus some pileup events which come from lower channels. Meanwhile, some of the real events at that energy were piled up to higher channels following the above empirical model. To make the pileup correction, we need to subtract pileup fractions from each channel and put them back where they belong, and remember each pileup photon came from two lower energy photons. These were done as follows: first multiply the CR(0-400) by the pileup rates given above to obtain the pileup fractions for that spectrum; for each channel N, we add the pileup fractions of channel N back to channel N, subtract one percent of pileup fractions of channel N from each channel $N + X$ ($X = 1$–$400$), and also add the same number to channel X; then just step along for the entire spectrum.

Figure 2 shows the SSX pileup corrections for the four spectra. In the top panel of each quadrant plot, the dots are the raw data, the solid line show the pileup corrected data. It is seen that when the spectra have sharp declines, the pileup corrections make the spectra even lower. The bottom panels show the ratio of the pileup corrected data vs. the raw data. The dashed vertical lines in the top panels indicate the position of six selected X-ray characteristic lines to be used to determine the energy scale of the spectra (see §5 and §11).

## 4 SSD FLAT FIELD TEST

In order to obtain the effective area by dividing the spectra of SSX and SS5, we need to know the relative Quantum Efficiency (QE) of the two SSDs as a function of energy. The SSD QE was measured as part of the HRMA calibration at both the XRCF and BESSY (electron storage ring in Berlin, Germany). This section discusses the SSD QE measurement made at the XRCF, i.e. the SSD C-continuum flat field test.

The C-continuum flat field test was done in June 1997, when the HRMA had been removed from the testing chamber and shipped to TRW. The two SSDs were swapped, SSX was placed at the SS5 location in building 500 and SS5 was placed at the focal plane. If the X-ray beam were uniform (this is not exactly the case – see §7), the X-ray flux at the two SSDs should be proportional to the inverse square of their distance to the source. The distance from the source to SSX was 38.199 m and to SS5 was 537.778 m. The 2 mm aperture was used for the SSX and 5 mm aperture was used for the SS5 for the flat field test.

Figure 3 shows the spectra, with counting rate as a function of spectral channel, obtained with the two SSDs. [2] There are several spectral peaks atop the continuum. The largest peak to the right of each spectrum is the pulser peak, which is used to estimate the pileup correction, as discussed in the previous section, and to calculate the deadtime correction (see §6). Other peaks are characteristic X-ray lines due to contaminations to the carbon anode (also seen in Figure 1). As the counting rates for the flat field test were very low (the SSX counting rate for the flat field test was about the same as the SS5 counting rate during the effective area measurements, see previous Section. The SS5 counting rate was 200 times lower than that of the SSX during the flat field test.), so the pileup effect is negligible.

# 5 SSD ENERGY SCALE

Using the characteristic X-ray lines atop the continuum spectra, the SSD energy scale can be determined. As shown in Figure 3, six strong and single peaked lines were selected to determine the energy scale. These six lines were identified to be, from left to right:

Table 2: X-ray Lines atop the C-continuum

| X-ray Line | Energy |
|---|---|
| Si-K$\alpha$, W-M$\alpha$ and W-M$\beta$ | 1.77525 keV * |
| Ca-K$\alpha$ | 3.69048 keV |
| Ti-K$\alpha$ | 4.50885 keV |
| V-K$\alpha$ ** | 4.94968 keV |
| Fe-K$\alpha$ | 6.39951 keV |
| W-L$\alpha$ | 8.37680 keV |

* The line center for Si-K$\alpha$, W-M$\alpha$ and W-M$\beta$ multiplet is weighted by line strength according to the HEG spectrum.
** Another choice for this line is Ti-K$\beta$ (4.93181 keV). We chose V-K$\alpha$ because this line has almost the same intensity as the Ti-K$\alpha$ line, while in the same spectrum all the $\beta$ lines are about an order of magnitude weaker than their $\alpha$ counterpart. Also V-K$\alpha$ gives a slightly better linear fit to the energy scale. Had Ti-K$\beta$ been chosen, the result is to lower the energy offset (parameter $a$ in Equation 1) by 0.003 keV, i.e. to decrease parameter $a$ in Table 3 and Table 5 by 0.003.

To determine the line centers, a Gaussian profile with a quadratic function base was fitted to each peak. The centers of fitted Gaussian are shown in Figure 3 as dashed vertical lines with the peaks. Each SSD energy scale is determined by fitting a linear least square fit of the line energies as a function of line centers:

$$Energy = a + b \cdot Channel \tag{1}$$

Figure 4 shows the energy to channel linear fit for the two SSDs. The fit is extremely good, as shown in Figure 5, which plots the residuals of the fits. Table 3 lists the fitted parameters.

Table 3: Flat Field Test SSD Energy Scale Linear Fit Parameters

| Detector | Spectral data | a | b |
|---|---|---|---|
| SSX | ss5_116414i000.pha | 0.0541744 | 0.00482999 |
| SS5 | ssx_116414i000.pha | 0.0464989 | 0.00502963 |

Using the above energy scales, the SSD spectra are converted from functions of channel to functions of energy and re-binned into equal energy bins. Figure 6 shows the C-continuum SSX and SS5 spectra as functions of energy, in units of counts per second per keV, where all the spectral lines are aligned up.

---

[2] Notice that the data file for SSX starts as 'ss5' and vice versa, because the two SSDs were swapped and the data files were named after the location of the detector.

# 6 SSD DEADTIME CORRECTION

In the raw data, the deadtime correction was automatically estimated, using a built-in circuitry and algorithms that follow the Gedcke-Hale formalism [2], and entered in the pha file header for each spectrum. However, for the SSDs, Gedcke-Hale formalism does not provide an accurate estimation because of low-level noise; the lower level discriminators were set very low to extend the SSDs' energy coverage as low as possible. A more accurate way to calculate the deadtime correction is to use the pulser method, in which artificial pulses are injected into the detector preamplifier to mimic real x-ray events. Since the pulses are processed just like X-rays – subject to interaction with hidden noise events, preamplifier reset pulses, *etc.* – the fraction of pulses that appear in the output spectrum is, to a good approximation, equal to the system livetime fraction. The formula applying the deadtime correction to SSD spectra using the pulser method is:

$$Actual\ counts = Measured\ counts \cdot \frac{Input\ pulser\ counts}{Measured\ pulser\ counts} \tag{2}$$

where the $Measured\ counts$ and $Measured\ pulser\ counts$ are from pileup corrected spectra.

Figure 7 illustrates how to determine the measured pulser counts. The top panel shows the SSX pulser spectrum from the SSD flat field test (see Figure 3). The bottom panel shows the SS5 pulser spectrum. Two vertical dotted lines surround the pulser peak indicate the pulser region. A power law is fitted to the spectrum outside the pulser region (100 channels below the left vertical line plus 100 channels above the right vertical line). The measured pulser counts equal the total counts under the pulser spectrum within the pulser region minus the total counts under the fitted power law spectrum within the pulser region. Since the counting rates are very low for the flat field test, the pileup effects are negligible. Later when we use the same method to do the deadtime corrections for the effective area measurements, we apply it to the pileup corrected data only.

For X-ray counting rate calculated using the pulser deadtime correction, the formula is:

$$\begin{aligned} Actual\ rate &= \frac{Measured\ counts}{TrueTime} \cdot Pulser\ deadtime\ correction && (3) \\ &= \frac{Measured\ counts}{TrueTime} \cdot \frac{Input\ pulser\ counts}{Measured\ Pulser\ counts} && (4) \end{aligned}$$

where $TrueTime$ is the full integration time which is listed in the pha file header as $\#trueTime\_sec$.

For the effective area, $A_{eff}(E)$, calculated using the SSX counts, $C_{SSX}(E)$, divided by SS5 counting rate, $C_{SS5}(E)$, the pulser deadtime correction is:

$$\begin{aligned} A_{eff} &= A_{eff}(w/o\ deadtime\ correction) \cdot \frac{SSX\ Pulser\ deadtime\ correction}{SS5\ Pulser\ deadtime\ correction} && (5) \\ &= A_{eff}(w/o\ deadtime\ correction) \cdot \frac{\left(\frac{SSX\ Input\ pulser\ counts}{SSX\ Measured\ pulser\ counts}\right)}{\left(\frac{SS5\ Input\ pulser\ counts}{SS5\ Measured\ pulser\ counts}\right)} && (6) \end{aligned}$$

# 7 BEAM UNIFORMITY TEST

We can obtain the relative quantum efficiency by dividing the two SSD spectra directly only if the X-ray beam intensities were exactly the same toward the directions of the two SSDs. But was the beam from the C-continuum source really uniform? To answer this question, a C-continuum beam uniformity test was made immediately after the C-continuum flatfield test (the flatfield test run ID is 116414, the beam uniformity test run ID is 116415).

During the beam uniformity test, the C-continuum source was operated in the same condition as for the flat field test, and the FPC-5 (i.e. the FPC detector in the Building 500) was scanned from the FPC-5 home position to the center (optical axis towards the HRMA), and to the SSD-5 home position, and then it scanned back in a reversed path. Two spectra were taken at each position. Taking the two spectra taken at the SSD-5 home position and dividing by the average of the two spectra taken on the optical axis, we obtain the relative flux ratio at those two positions as a function of energy (with low spectral resolution). Figure 8 show the relative flux ratio. It is seen that the beam is close to but not exactly uniform. It varies between 1.00 and 1.02. The solid curve in Figure 8 is a quadratic fit to the data. This is purely an empirical model which fits the data very well. The reduced $\chi^2$ is 1.01652. So the beam uniformity as a function of energy can be well represented using this quadratic function, with a relative error of 0.0034:

$$FR = 1.01341 - 0.00512E + 0.000567E^2 \tag{7}$$

where $FR$ is the flux ratio of at SS5 position vs. on the optical axis, and $E$ is the X-ray energy in unit of keV.

# 8 SSD RELATIVE QUANTUM EFFICIENCY

With all above considerations, we now finally can obtain the relative quantum efficiency of the two SSDs. The SS5/SSX quantum efficiency ratio, $R(E)$, is:

$$\begin{aligned} R(E) \quad = \quad & \frac{C_{SS5\ flatfield}(E)}{C_{SSX\ flatfield}(E)} \cdot \frac{SS5\ pulser\ deadtime\ correction}{SSX\ pulser\ deadtime\ correction} \cdot \\ & \frac{(SS5\ to\ source\ distance)^2}{(SSX\ to\ source\ distance)^2} \cdot \frac{SSX\ aperture\ area}{SS5\ aperture\ area} \cdot \\ & (Beam\ flux\ ratio\ between\ SS5\ position\ and\ optical\ axis) \end{aligned} \tag{8}$$

where

- $C_{SS5\ flatfield}(E)$ and $C_{SSX\ flatfield}(E)$ are counts as functions of energy for the two SSDs from the flatfield test (see Figure 6).
- Using the method discussed in §6, the pulser deadtime corrections are calculated to be 1.0092 and 1.0569 for SS5 and SSX, respectively.
- The source to SSD distances are 537.778 m and 38.199 m for SS5 and SSX, respectively. Errors on the distance measurements are negligible for this calculation.
- For the flat field test, the apertures used were 2 mm (actual diameter = 1.9990 ± 0.0073 mm) for SSX. and 5 mm (actual diameter = 4.9962 ± 0.0073 mm) for SS5. The combined relative error due to the two aperture area uncertainties is 0.0079.
- For the beam flux ratio, measured with FPC-5, we use Equation 7.

Figure 9 shows the SS5/SSX QE ratio, $R(E)$, as a function of energy. The top panel show the QE ratio calculated using formula (8). $R(E)$ is near unity for energies above 2 keV as expected. $R(E)$ varies drastically for energies below 2 keV, because of the icing effect (see the following section). In this case, there was more ice on the SSX therefore there was much higher transmission for SS5. A wiggle around line 1.775 keV indicates that the two SSDs have slightly different spectral resolution.

This $R(E)$ curve is rather noisy. In the bottom panel, the data were binned into 0.3 keV bins and fitted to a flat ratio for energies above 3 keV (since at energies between 2 and 3 keV, the ratio was still slightly effected by the icing). The fit is very good, with a ratio of 1.0141 ± 0.0021 and $\chi^2_\nu = 1.0897$. Here the error, 0.0021, is only the standard deviation of the mean of the binned flat field data in the 3–10 keV band. The total error for the quantum efficiency ratio also includes the beam uniformity error (0.0034) and the aperture size error (0.0079). Adding them in quadrature, the total relative error is 0.0088.

Because of the icing effect, the flat field test can only provide us with this ratio within 3–10 keV band. Since this ratio is reasonably energy independent, we assume, for the entire 0–10 keV energy band, the SS5/SSX quantum efficiency ratio is: [3]

$$R(E) = 1.0141 \pm 0.0089 \tag{9}$$

---

[3] Because this ratio is energy independent, a large portion of the offset from unity is probably due to the combined aperture size error (0.0079). Because the aperture wheels were built into the SSD system, the apertures moved with the SSDs when the two SSDs were swapped during the flat field test. The measured SS5/SSX quantum efficiency ratio reflects a combination of real QE ratio of the SSDs and the aperture area ratio. In any case, the result of $R = 1.0141 \pm 0.0089$ provides the correct QE ratio for the effective area measurements.

# 9 SSD ICING EFFECT

In this section we discuss the so called SSD icing effect which we encountered in the previous section. Because SSD was cooled to liquid nitrogen temperature, even in its vacuum container, there was still a small amount of trapped water which condensed on the surface of the SSD to form a very thin layer of ice. This thin ice layer decreases the transmission of low energy X-rays.

In order to monitor the ice build up, a radioactive isotope $^{244}_{96}$Cm excited Fe source was placed on the aperture wheel and rotated in front of the SS5 from time to time. The Figure 10 shows the Fe-L$\alpha$ (0.705 keV) and Fe-K$\alpha$ (6.40 keV) line intensity with error bars measured with SS5 as a function of time from 960824 to 970521 (JD 2450320 - 2450590). The SSD C-continuum measurements were made in the middle of that period on 970113 and 970130. In the top panel, the Fe-L$\alpha$ intensity has two peaks, on 961031 and 970223, followed by declines. These two peaks indicate the time when the SS5 was warmed up and we assume there was no ice then. The declines indicate the ice build up, reducing the transmission of Fe-L$\alpha$ into the SS5. In the bottom panel, the fluctuations of Fe-K$\alpha$ intensity could be due to icing, source aging and other temporal variations. To obtain the icing information, we only need to focus on the intensity ratio of Fe-L$\alpha$/Fe-K$\alpha$. Data from Figure 10 are listed in Table 4: At the end of each ice build up period, the Fe-L$\alpha$/Fe-K$\alpha$ transmission ratio is 74% of its initial value. This result can be used to obtain the ice thickness.

Table 4: SSD-500 Icing Data

| Icing Period | | Fe-L$\alpha$ Intensity | Fe-K$\alpha$ Intensity | Intensity ratio |
|---|---|---|---|---|
| First Period | Begin | 34.2 | 90.8 | 0.3767 |
| 961031 - 970129 | End | 24.5 | 87.9 | 0.2787 |
| End/Begin Ratio | | | | 74.00 % |
| Second Period | Begin | 32.0 | 87.1 | 0.3673 |
| 970223 - 970514 | End | 23.5 | 86.5 | 0.2717 |
| End/Begin Ratio | | | | 73.97 % |

Figure 11 shows the X-ray transmission of ice. The solid line is a fit with Fe-L$\alpha$ (0.705 keV) line transmission being 74% of Fe-K$\alpha$ (6.40 keV) line transmission. The result is a 0.3 $\mu$m ice layer. For reference, a transmission curve of a 1$\mu$m ice layer is plotted as a dotted line. According to this fit, during the calibration, the thickest ice build up on SS5 was 0.3 $\mu$m, at around 970129 and 970514. At other times, the ice was thinner. The SSX did not have a $^{244}_{96}$Cm source, so we do not have any data about the icing on the SSX.

Figure 11 tells us that icing has less than 0.7% effect for energies over 3 keV. At 2 keV, it can decrease the X-ray transmission by up to 2%. At the same time, icing has very severe effect for energies below 2 keV. Because the ice build up is a function of time and the build up on two SSDs could be different, the SSD data below 2 keV are not reliable. We have seen an indication of that in the previous section (see Figure 9). So in the flat field data analysis and in the following effective are data, we will not use the SSD spectra at low energies.

# 10 BACKGROUND

During the HRMA calibration, background runs were taken almost every day when the source valve was closed and all the detectors were turned on. To evaluate the effect of the background on the SSD C-continuum measurements, we examined all the SSD background spectra and found that the background is extremely low.

Figure 12 shows a pair of typical SSD background spectra. It was taken on 970124, with TRW ID D-IXF-BG-1.021, run ID 110036 and integration time of 2100 seconds. They are summed spectra of seven background runs of 300 seconds each. It is seen that, other than the pulser peak at near channel 2400 and some electronic noise near channel 60, the spectra are very clean in the region to be used to reduce the HRMA effective area (channels 100–2000). The average counts per channel per second are 0.000046 and 0.000024 for SSX and SS5, respectively. For all the background spectra, the average counting rate in channels 100–2000 ranges from 0.000019 to 0.000098 c/s/ch. This level of background is negligible in our data analysis.

# 11 DATA ANALYSIS AND REDUCTION

With all the above considerations, we can now obtain the HRMA effective area. The four Phase-E SSD effective area measurements for the four shells have TRW IDs of E-IXS-MC-15.001,2,3,4 and run IDs 110539, 110540, 110541, and 110542. The "MC" in TRW ID stands for molecular contamination measurements, but they also serve as on-axis effective area C-continuum measurements.

We start with the pileup corrected SSX and SS5 spectra (see §3). In Figure 2, the upper panels show the pileup corrected SSX and SS5 spectra. The SSD energy scale was determined using the six characteristic X-ray lines atop the continuum spectra, indicated by dashed vertical lines, as discussed in §5. First a Gaussian profile with quadratic function was fitted to each peak to determine the line center. The fitted centers for the same line in different spectra of the same SSD differ only by a couple of channels, which is well within the fitted errors. So an averaged center for each line from the four measurements was used to obtain the energy scale. The energy scales of SSX and SS5 are determined by doing a linear least squares fit of the averaged line centers to the line energies using the simple linear Equation (1).

Figure 13 shows the energy to channel linear fit for the two SSDs. The fit is extremely good, as shown in Figure 14, which plots the residuals of the fits. Table 5 lists the fitted parameters for the two SSDs. The energy scale is slightly different from that of the flat field test.

Table 5: Effective Area Measurements SSD Energy Scale Linear Fit Parameters

| Detector | Spectral data | a | b |
|---|---|---|---|
| SSX | ssx_110539,540,541,542i000.pha | 0.0547638 | 0.00490269 |
| SS5 | ss5_110539,540,541,542i000.pha | 0.0443109 | 0.00508020 |

Using the linear fit parameters listed in Table 5, each of the eight SSD spectra was scaled as a function of energy. Then they were binned into equal energy bins by dividing the spectra by the fitting parameter $b$ in Table 5. The pulser deadtime corrections are also applied to the spectra the same way as to the flat field data. The results are four pairs of SSX and SS5 spectra as functions of energy, keV, and in units of counts/second/keV. They are shown in the top and middle panels of each quadrant plot in Figure 15. The dashed vertical lines indicate the six X-ray lines used for energy scaling.

# 12 EFFECTIVE AREA

The HRMA effective area at the XRCF is defined to be the photon collecting area in the plane of the HRMA pre-collimater entrance, which is 1491.64 mm forward from CAP Datum-A (the front surface of the Central Aperture Plate), i.e. 526.01236 meters from the source.[4]

For the C-continuum SSD measurements, the HRMA mirror effective area, $A_{eff}(E)$, is:

$$A_{eff}(E) = \frac{C_{ssx}(E)}{C_{ss5}(E)} \cdot \frac{PDC_{ssx}}{PDC_{ss5}} \cdot \frac{D^2_{hrma}}{D^2_{ss5}} \cdot A_{ss5} \cdot R(E) \qquad (10)$$

where

- $C_{ssx}(E)$ and $C_{ss5}(E)$ are the SSX and SS5 spectra with the correct energy scale and equal energy bins (in units of counts/second/keV).
- $PDC_{ssx}$ and $PDC_{ss5}$ are the pulser deadtime corrections for the SSX and SS5.
- $D_{hrma}$ = 526.01236 meter is the distance from the source to the HRMA pre-collimater entrance, where the effective area is defined.

---

[4] This definition is necessary because of the diverging X-ray beam at the XRCF. It is not necessary for on-orbit case as the X-rays are parallel and the effective area is the same in any plane.

- $D_{ss5}$ = 38.199 meters is the distance from the source to SS5.
- $A_{ss5}$ is the SS5 aperture area. A 2 mm aperture was used for all the measurements. Its actual equivalent diameter is 1.9990 ± 0.0073 mm. So $A_{ss5} = 0.031385 \pm 0.00023$ cm$^2$
- R(E) = 1.0141 ± 0.0089 is the relative SS5/SSX quantum efficiency from the flat field test.

Because each of the SS5 spectra are rather noisy, four SS5 spectra are averaged to make $C_{ss5}(E)$, which has the noise reduced by a factor of two. The source intensity was stable enough during these four measurements so the temporal fluctuation is negligible. The $C_{ssx}(E)$ and $C_{ss5}(E)$ are obtained using the method discussed in the previous Section. The $PDC_{ssx}$ and $PDC_{ss5}$ are obtained using the method discussed in §6 and listed in Table 6.

Table 6: Effective Area Measurements SSD Pulser Deadtime Corrections

| Run ID | $\mathrm{PDC}_{ssx}$ | $\mathrm{PDC}_{average\ ss5}$ | $\mathrm{PDC}_{ssx}/\mathrm{PDC}_{average\ ss5}$ |
|---|---|---|---|
| 110539 | 1.11827 | 1.01651 | 1.10011 |
| 110540 | 1.10408 | 1.01651 | 1.08615 |
| 110541 | 1.09579 | 1.01651 | 1.07799 |
| 110542 | 1.07069 | 1.01651 | 1.05330 |

The bottom panels of each quadrant plot in Figure 15 show the effective area results according to equation 10. The six vertical dashed lines are the six energy lines used to determine the energy scale. Each effective area curve was binned into 0.1 keV energy bins. According to the SSD energy scale, there are 20 channels in each energy bin. The plotted error bars are the standard deviation of the mean in the energy bins. Systematic errors such as the SS5 aperture area uncertainly (0.0073) and the SSD quantum efficiency ratio error (0.0088) are not included in these four plots but will be included later in the final results.

# 13 ERRCR ANALYSIS

The error of the HRMA effective area is:

$$\sigma_{ea} = (\sigma_{e-bin}^2 + \sigma_{2mm-ap}^2 + \sigma_{qe}^2)^{1/2} \tag{11}$$

where

| | | |
|---|---|---|
| $\sigma_{e-bin}$ | Standard deviation of the mean in each 0.1 keV bin of the SSD spectra | ~1–4% |
| $\sigma_{2mm-ap}$ | Uncertainty of the SS5 2 mm aperture area (0.031385 ± 0.00023 cm$^2$) | 0.73% |
| $\sigma_{qe}$ | Error of the SSD quantum efficiency ratio (1.0141 ± 0.0089) | 0.88% |
| $\sigma_{ea}$ | Effective area error | ~1.3–4% |

For the effective area of the entire HRMA, the absolute errors are the quadrature sum of the absolute errors from the four shells. Therefore its relative errors are reduced accordingly, to ~0.7–3.6%.

# 14 COMPARING MEASUREMENTS WITH RAYTRACE

Figure 16 compare the measured effective area with the raytrace prediction within a 2 mm aperture for each mirror shells. In the top panel of each quadrant plot, the solid line is the raytrace prediction, the dotted line is the SSD measured effective area with the C-continuum source, which is the same as plotted in the bottom panel of Figure 15. As mentioned before, the SSD data below 2 keV (most parts are higher than the raytrace prediction) should be ignored due to the icing effect. The FPC spectral line data are also plotted in the figures for comparison.

For energies above 2 keV, the data are significantly below the prediction, especially for shell 1. The bottom panel of each quadrant plot in Figure 16 show the effective area ratio of data/raytrace. It is seen that for shell 1, the data is about ~10–15% less than the prediction at 2–4 keV and ~15–30% less than the prediction for shell 1 at 4–6 keV. For other shells the discrepancies are less than 15%.

Figure 17 shows the full HRMA effective area data with the raytrace prediction within a 2 mm aperture. The SSD C-continuum data and four of the seven FPC line spectral data (0.277 keV, 1.49 keV, 4.51 keV and 6.40keV) are the sums of data from the four shells. The SSD line spectral data and three of the seven FPC line spectral data (0.93 keV, 5.41 keV and 8.03 keV) are the direct measurements of the full HRMA. The data are below the raytrace prediction by $\sim$5–10% in the 2–10 keV band. In the raytrace prediction, there is a dip near the Ir M-edge (2.05 keV). The SSD C-continuum data could not reveal it due to the finite spectral resolution of the SSD. However, the SSD spectral line measurement at the 2.16 keV (Nb-L) did show a dip. The fluctuations in the EA ratio curves near the Ir M-edge in the 2.0–2.3 keV region are also due to the finite spectral resolution of the SSD.

In Figures 16 and 17, most of the FPC line data are below the SSD continuum data. Presently we do not know the exact cause of this. We hope to resolve this discrepancy as this work progresses.

## 15 CALIBRATING THE HRMA EFFECTIVE AREA

The XRCF HRMA effective area raytrace predictions were originally generated based on the HRMA model which is accurate to the best of our knowledge, including the HRMA tilt and decenter measured during the calibration. However, as we can see in the previous section, the calibration data show that for energies higher than 2 keV, the measured effective area is substantially less than the predicted effective area by well more than the experimental errors, especially for shell 1. At least part of this discrepancy is due to differences in the way the raytrace model calculates reflectivity, compared to our derivation of optical constants via our synchrotron measurements. There are also some discrepancies between the mirror surface roughness scattering model and the data measured from the wing scan measurements. We are currently assessing and correcting for these differences. For the present, based on the principle that theory should yield to the experiment, we use the XRCF calibration data to scale down the raytrace empirically for both on-orbit and XRCF HRMA effective area predictions.

In order to smooth the Poisson noise in the correction factor, a fourth order polynomial is used to fit the deficit curve of the effective area ratio between 2.3 keV and 10 keV. The polynomial fit curves for the four shells and the HRMA are plotted as solid curves in the data/raytrace ratio plots in Figures 16 and 17. These polynomials as functions of energy are to be used to scale the raytrace prediction. For higher energies where the effective area drops to below a few cm$^2$ (i.e. $\geq$6.7 keV for shell 1, $\geq$7.9 keV for shell 3, and $\geq$9.0 keV for shell 4), there are not enough data to make a reasonable fit, and a ratio of unity is used.

Since the SSD data are not reliable for lower energies, FPC spectral line data for energies below 2.3 keV are used for scaling. The average ratios between the FPC data and the raytrace are used as the scaling factor. They are 1.0234 , 0.9983, 0.9998, 1.0136, and 1.0055, for shells 1,3,4,6 and the HRMA, respectively.

The errors for the scaling factors are:

| | | |
|---|---|---|
| $E < 2.3$ keV: | FPC measurement errors | 0.3–1.9% |
| | Deviations of the FPC data from the scaling factor | 0.7–3.2% |
| | Statistical errors from raytrace simulation | <0.3% |
| | Total scaling factor errors | $\sim$1.1–3.4% |
| $E \geq 2.3$ keV: | Standard deviation of the polynomial fit | 1.7–3.3% |
| | Deviation of each data point from the polynomial fit | 0.2–6.0% |
| | Statistical errors from raytrace simulation | <0.3% |
| | Total scaling factor errors | $\sim$2–7% |

## 16 HRMA EFFECTIVE AREA RAYTRACE PREDICTIONS

The original raytrace predictions of the HRMA effective area for both the on-orbit and at XRCF cases were generated based on the HRMA model. The HRMA model includes mirror tilts and decenters measured at Kodak and XRCF, mirror low frequency surface maps from the HDOS metrology measurements, mirror CAP, pre- and post-collimators, apertures, ghost baffles, and mirror distortion due to epoxy cure shrinkage. For the XRCF case, the HRMA model also includes the finite source distance at the XRCF and the mirror distortion due to gravity.

The reflectivities are based on: [5] E < 2 keV: Gullikson '95 optical constant table. [3]; E ≥ 2 keV: AXAF mirror witness flat synchrotron measurements made by Graessle et al. [4]

The mirror surface roughness scattering is based on the Power Spectral Density (PSD) produced from the HDOS metrology measurements and calculated with a program "foldw1" written by Leon Van Speybroeck, which is based on the scattering theory by Beckmann and Spizzichino. [5]

Figures 18 and 19 show the raytrace predicted effective areas and encircled energies of shell 1 and the HRMA at the XRCF. The top panels shows the effective area curves within 2 mm, 35 mm diameter apertures, and $2\pi$ steradians. The bottom panels show the encircled energies of 2 mm and 35 mm apertures as fractions of that within $2\pi$ steradians. Figures 20 and 21 show the raytrace predicted effective areas and encircled energies of shell 1 and the HRMA on-orbit.

The purpose of showing these figures is to compare the encircled energy curves between the XRCF and the on-orbit cases. Since the SSD C-continuum effective area data we reduced are for only 2 mm aperture, we should be able to use these data to scale down the raytrace predicted XRCF effective area curve within 2 mm diameter. How about the XRCF effective area within larger apertures and $2\pi$ steradians? How about the on-orbit cases? Can we use the XRCF 2 mm aperture measurement to scale down other effective area curves the same way?

Let's first look at the XRCF cases. The fractional encircled energy within 2 mm aperture varies as a function of energy and from shell to shell. For shell 1 at 6.5 keV, it can be as low as 86% (see Figure 18). For other shells (not shown), the fractional encircled energy curve are all higher than 92%. Can we use the 2 mm aperture data to scale down the effective area within larger apertures and $2\pi$ steradians? The short answer is "we don't know", because we still don't know the exact cause or causes of the discrepancy between the data and the model. But we have some FPC spectral line measurements using the 35 mm diameter aperture. The data disagree with the raytrace prediction by about the same amount as the 2 mm aperture data did. The fractional encircled energy within 35 mm aperture is more than 99% for almost all the shells and all energies (see Figures 18 and 19). Therefore with good confidence we should be able to use the 2 mm aperture data to scale down the XRCF effective area within larger apertures as well as within the $2\pi$ steradians.

Next let's look at the on-orbit cases. The effective area and fractional encircled energy curves are very similar to the same curves for the XRCF cases. Therefore we can, with the same confident level, scale down the on-orbit HRMA effective area prediction curve the same way as for the XRCF cases.

Therefore, we will use the 2 mm aperture calibration data to scale down the raytrace predicted effective areas within any apertures greater or equal to 2 mm diameter for both on-orbit and at XRCF cases.

## 17 XRCF HRMA EFFECTIVE AREA

Figures 22 and 23 show the XRCF HRMA and four shells effective areas within 2 mm diameters and $2\pi$ steradians, for the original raytrace and the calibrated curves with errors estimated in §15.

These are our current best estimates for the HRMA effective area at the XRCF. Other calibration teams can use these data to calibrate their instruments. The "rdb" tables of the XRCF HRMA effective area, as well as Figures 22 and 23, can be accessed on the WWW page: http://hea-www.harvard.edu/MST/mirror/www/xrcf/hrma_ea.html, or are available from the first author.

## 18 ON-ORBIT HRMA EFFECTIVE AREA PREDICTION

Figures 24 and 25 show the on-orbit HRMA and four shells effective areas within 2 mm diameters and $2\pi$ steradians, [6] for the original raytrace and the calibrated curves with errors estimated in §15.

---

[5] Because we used different optical constant tables for E < 2 keV and E ≥ 2 keV for the raytracing, there is a discontinuity at 2 keV in all the raytrace effective area curves. Obviously this discontinuity is not real and the optical constant in two tables should agree at 2 keV. We are currently working to resolve this discrepancy.

[6] Although it is not possible to use just a single shell on-orbit, the HETG operations require the effective area predictions for Shells 1+3 and Shells 4+6 separately.

These are our current best on-orbit effective area predictions for the HRMA. They can be used to make AXAF on-orbit performance predictions. The "rdb" tables of the predicted on-orbit HRMA effective area, as well as Figures 24 and 25, can be accessed on the WWW page: http://hea-www.harvard.edu/MST/mirror/www/orbit/hrma_ea.html, or are available from the first author.

# 19 CONCLUSION

The HRMA calibration at the XRCF of MSFC made novel use of the X-ray continuum radiation from a conventional electron-impact source. Taking advantage of the good spectral resolution of solid-state detectors, continuum measurements proved advantageous in calibrating the effective area of AXAF's High-Resolution Mirror Assembly (HRMA) for the entire AXAF energy band.

The HRMA effective area was obtained by comparing the spectrum detected by a SSD at the focal plane with the spectrum detected by a beam normalization SSD in Building 500. Many systematic effects such as pileup, deadtime, beam uniformity, energy scale, icing, relative quantum efficiency, background, *etc.*, must be analyzed during the data reduction process.

In the data analysis, we did not use the actual SSD spectral response matrices. This could introduce an error as the energy resolutions of the two SSDs are slightly different. However, we did convolutions of the preliminary SSD spectral response matrices with the calibration data scaled raytrace predictions, and compared them with the measured effective area for each shell. The fit was reasonably good. Had we used the original raytrace prediction in the convolution, the fit would not be acceptable. This justifies the method we used to reduce the data and the calibrated effective area we generated. This work will be improved in the near future by using more detailed SSD response matrices calibrated at the BESSY to unfold the spectra and a pileup correction model as a continuous function of energy.

The results of the SSD C-continuum measurements show that the measured effective area is substantially less than the predicted effective area by well more than the experimental errors, especially for shell 1. Although we still don't have a good explanation for the cause or causes of this discrepancy on this important AXAF capability, we are currently assessing the reflectivity and surface scattering calculations in our raytrace model. When this is done, we will re-assess the differences between the data and the model, and, if necessary, apply similar, but smaller, polynomial corrections to our improved raytrace predictions.

Presently we have yet to achieve the calibration goal of 1% precision for the HRMA effective area. We expect to approach this goal as this work progresses.

Based on the SSD C-continuum Measurements at the XRCF, we have calibrated the HRMA effective area for its on-orbit performance as well as its actual values at the XRCF. The HRMA effective area is one of the most important AXAF capabilities. These calibrated values of the effective area can be used to make AXAF on-orbit performance predictions, and by other AXAF teams to calibrate their science instruments.

The HRMA effective area "rdb" tables and their figures are available, as of this writing, on the following World Wide Web pages, and also available from the first author.

XRCF: *http://hea-www.harvard.edu/MST/mirror/www/xrcf/hrma_ea.html*
On-orbit: *http://hea-www.harvard.edu/MST/mirror/www/orbit/hrma_ea.html*

# 20 ACKNOWLEDGMENTS

The successful ground calibration of the AXAF owes to the hard work of hundreds of people. We would like to thank many scientists, engineers, and other personnel from many organizations including NASA, SAO, MIT, PSU, TRW, EKC, HDOS, OCLI, SRON and MPE who have made this work possible.

This work was supported in part by NASA grant NAG8-792 and NASA contract NAS8-40224.

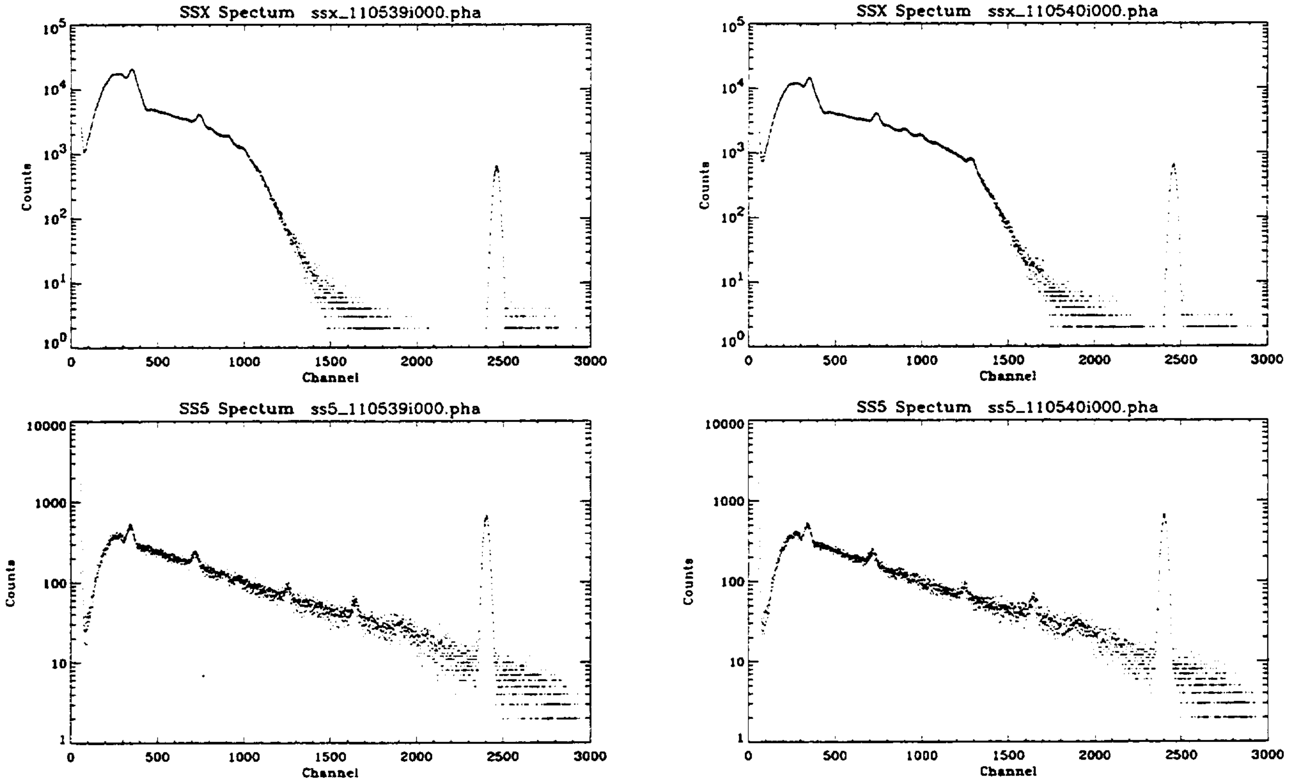

SSX and SS5 spectra: Shell 1; Run ID 110539.

SSX and SS5 spectra: Shell 3; Run ID 110540.

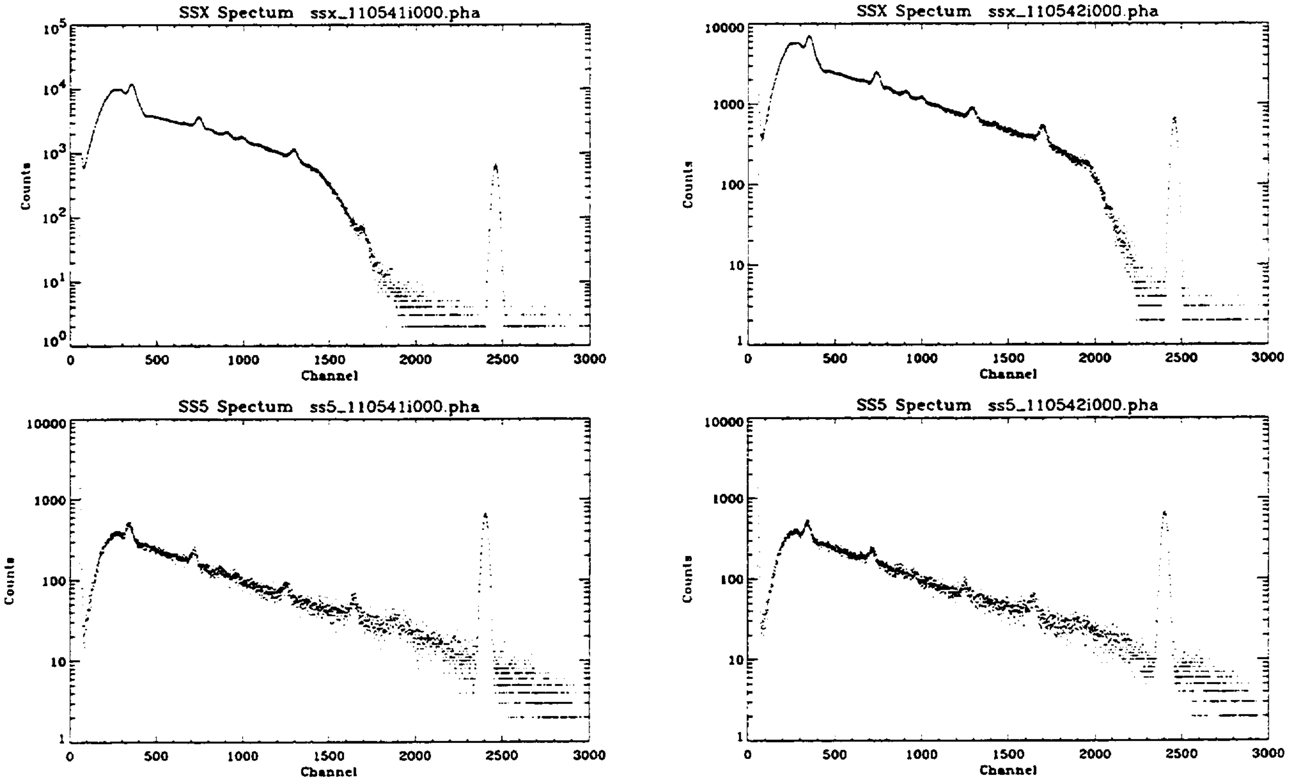

SSX and SS5 spectra: Shell 4; Run ID 110541.

SSX and SS5 spectra: Shell 6; Run ID 110542.

Figure 1: C-continuum SSX and SS5 spectra of four HRMA shells. Aperture: 2 mm; Integration time: 1000 seconds.

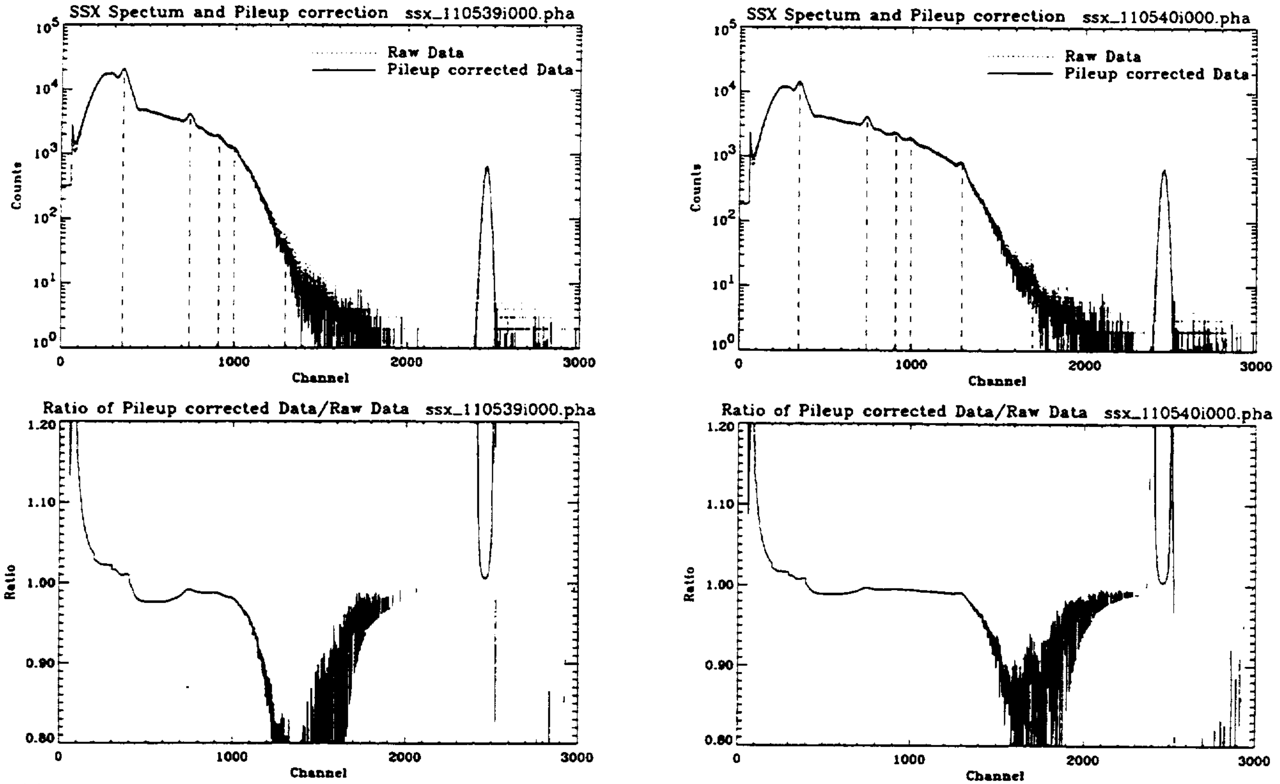

SSX pileup correction: Shell 1; Run ID 110539.

SSX pileup correction: Shell 3; Run ID 110540.

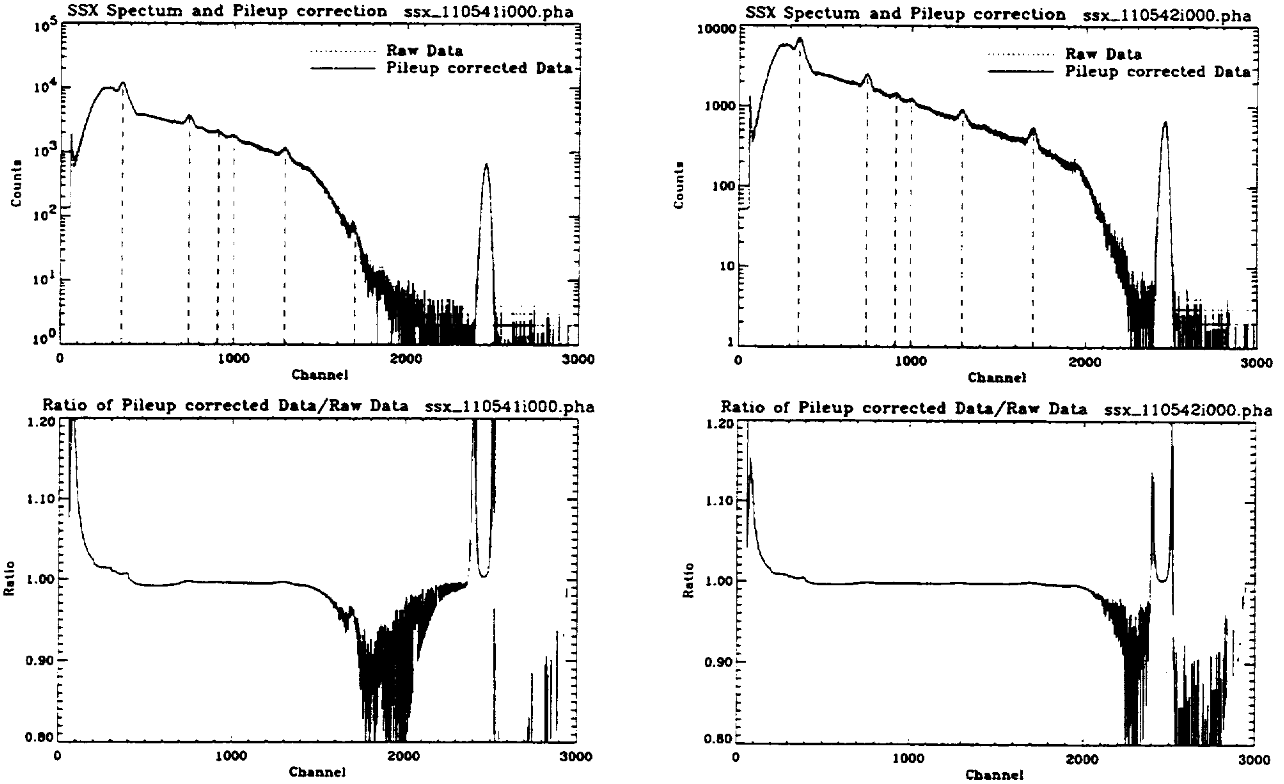

SSX pileup correction: Shell 4; Run ID 110541.

SSX pileup correction: Shell 6; Run ID 110542.

Figure 2: SSX spectra and pileup correction of four shells. Upper panel of each quadrant plot show the raw data and pileup corrected data. Lower panel shows the ratio of pileup corrected data to the raw data.

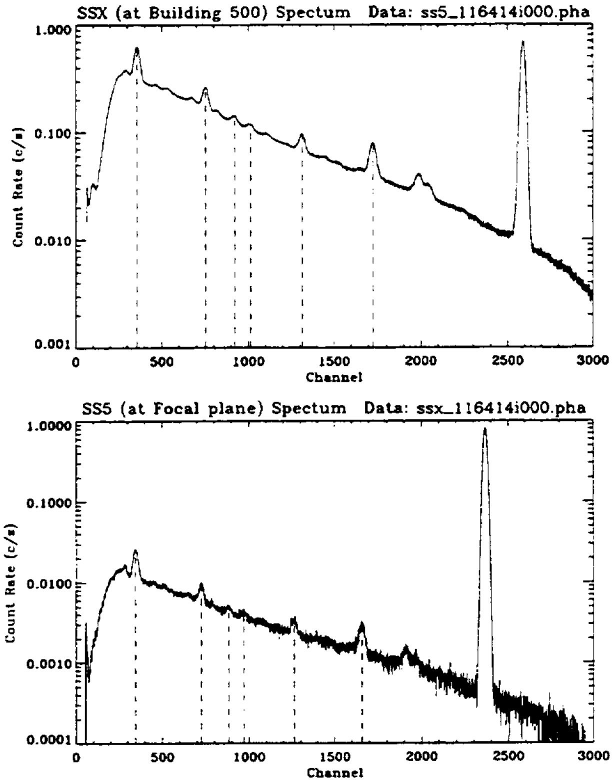

Figure 3: C-continuum flat field test SSX and SS5 spectra. Run ID: 116414. 57600 seconds. Dashed vertical lines indicate fitted centers of X-ray characteristic lines to be used for calibrating the SSD energy scale.

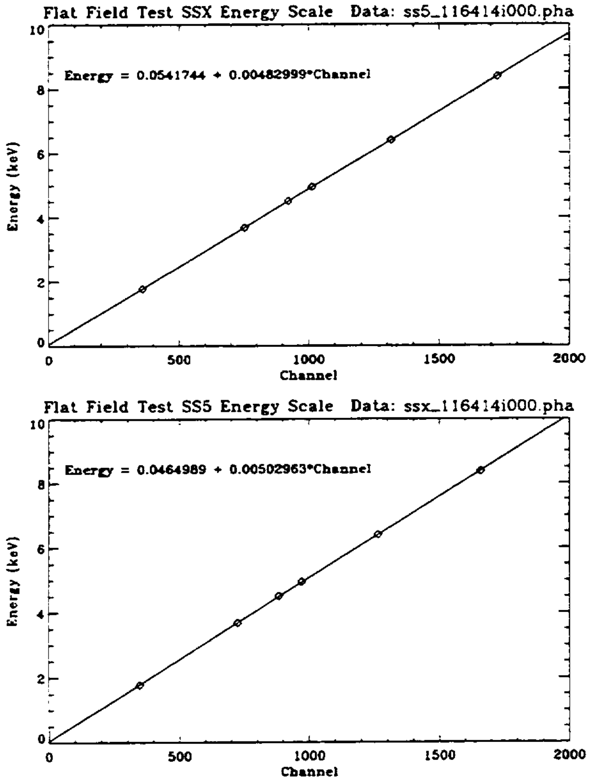

Figure 4: SSX and SS5 energy scales for the flat field test, fitted with six X-ray line energies.

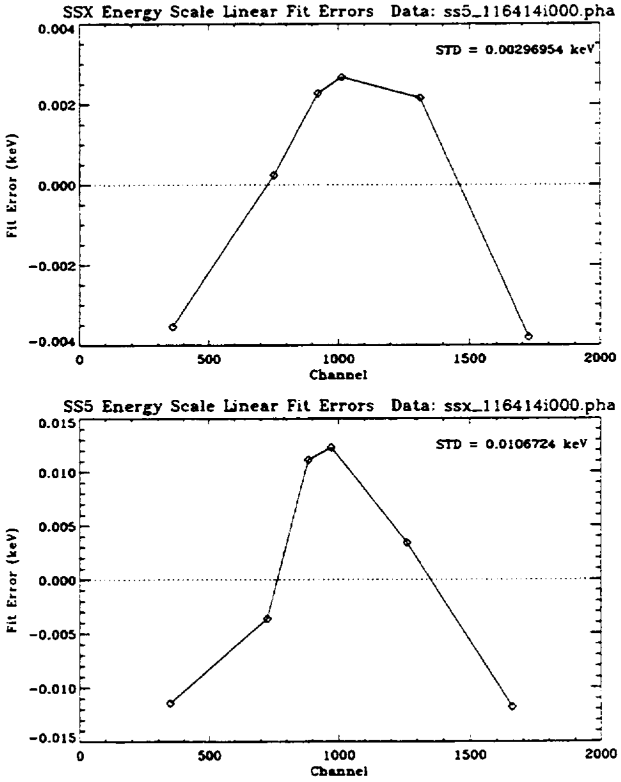

Figure 5: SSX and SS5 energy scale linear fit residuals for the flat field test.

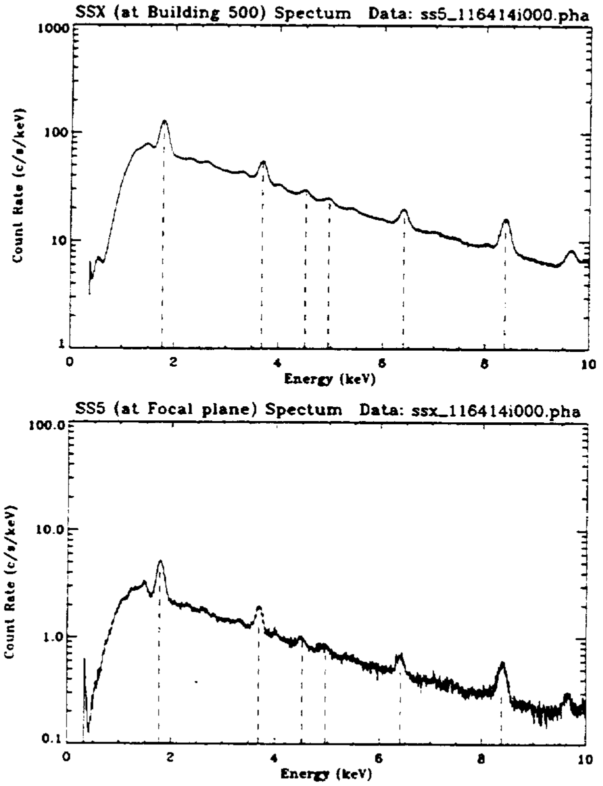

Figure 6: C-continuum flat field test SSX and SS5 spectra as functions of energy, using energy scales from Figure 4.

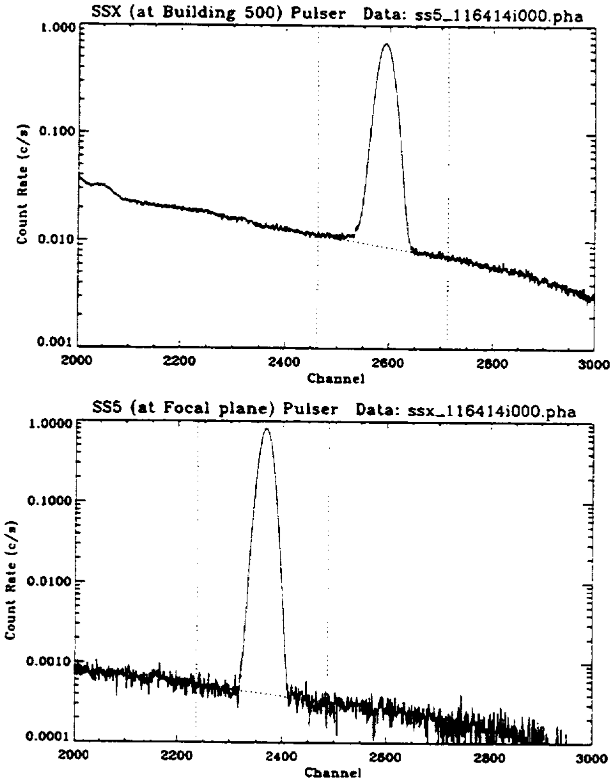

Figure 7: SSX and SS5 pulser spectra. Two vertical dotted lines indicate the pulser region. A dotted line under the peak is the power law fit to the continuum.

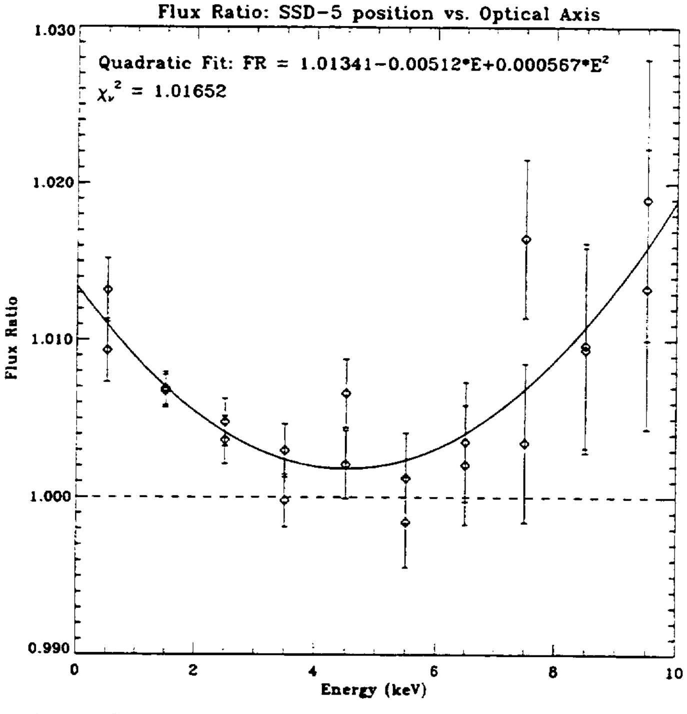

Figure 8: C-continuum FPC-5 beam flux ratio - SSD-5 position vs. optical axis - as a function of energy. Data are fit to a quadratic function.

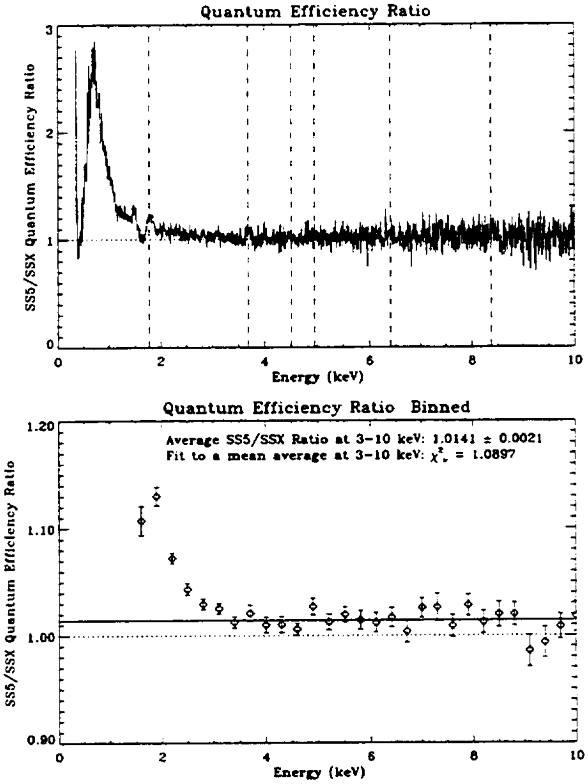

Figure 9: SS5/SSX quantum efficiency ratio. In the top panel, the large ratio below 2 keV is mainly due to the different ice build up on the two detectors. The bottom panel shows the ratio curve binned and fitted to a constant ratio. The solid line is the average ratio at 3–10 keV.

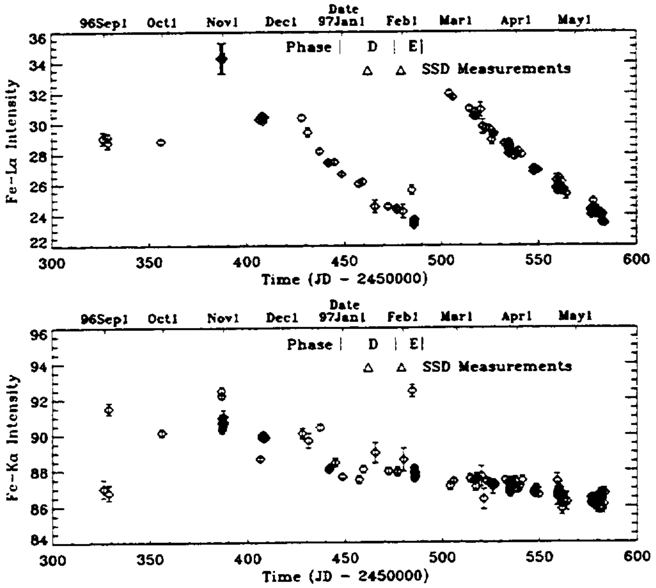

Figure 10: SS5 data of Fe-L$\alpha$ and Fe-K$\alpha$ lines from a $^{244}_{96}$Cm excited Fe source, used to estimate the ice thickness.

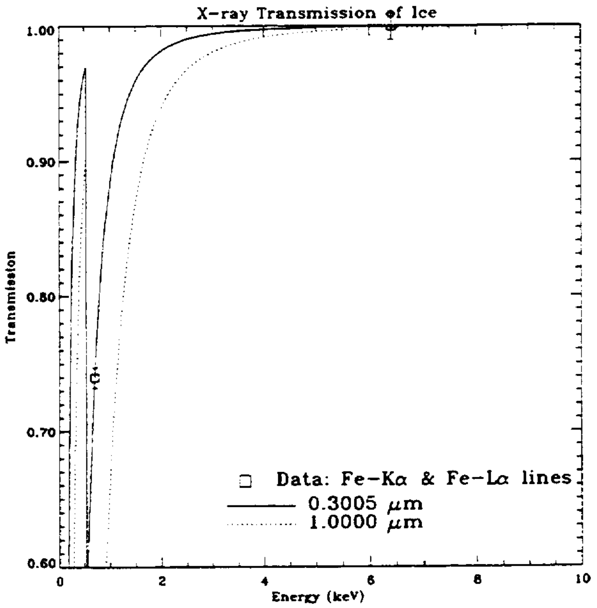

Figure 11: X-ray transmission of ice. The solid line is a fit with Fe-L$\alpha$ (0.705 keV) line transmission being 74% of Fe-K$\alpha$ (6.40 keV) line transmission. The result is a 0.3 $\mu$m ice layer.

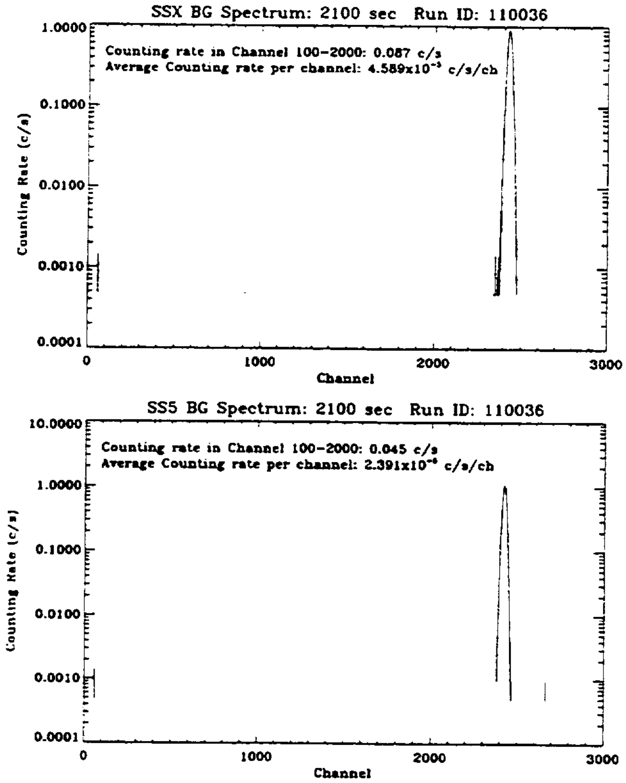

Figure 12: SSX and SS5 spectra of background run. Date: 970124; Run ID: 110036; 2100 seconds.

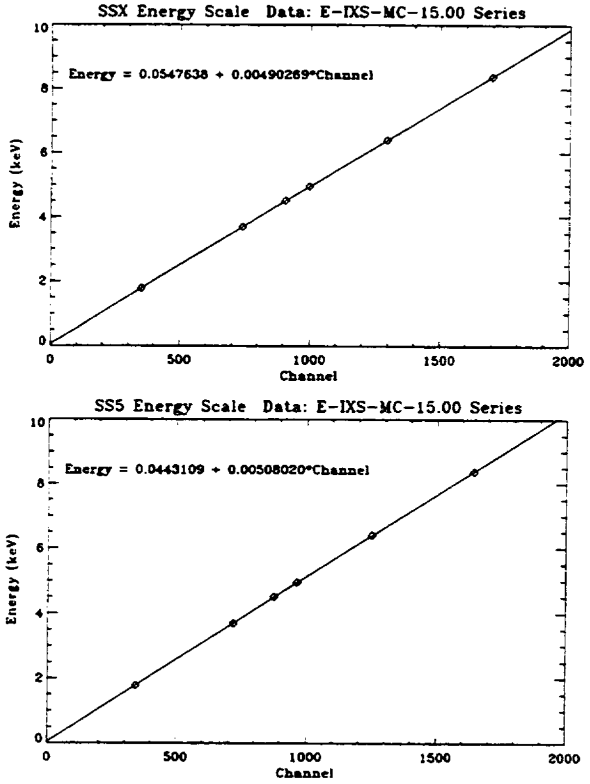

Figure 13: SSX and SS5 energy scales for the effective area measurements, fitted with six X-ray line energies, averaged over four spectra.

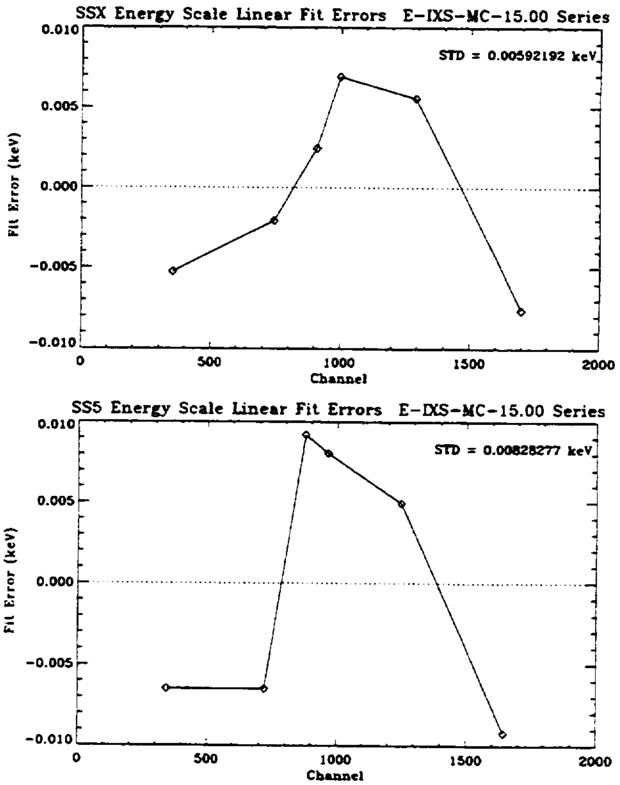

Figure 14: SSX and SS5 energy scale linear fit residuals for the C-continuum effective area measurements.

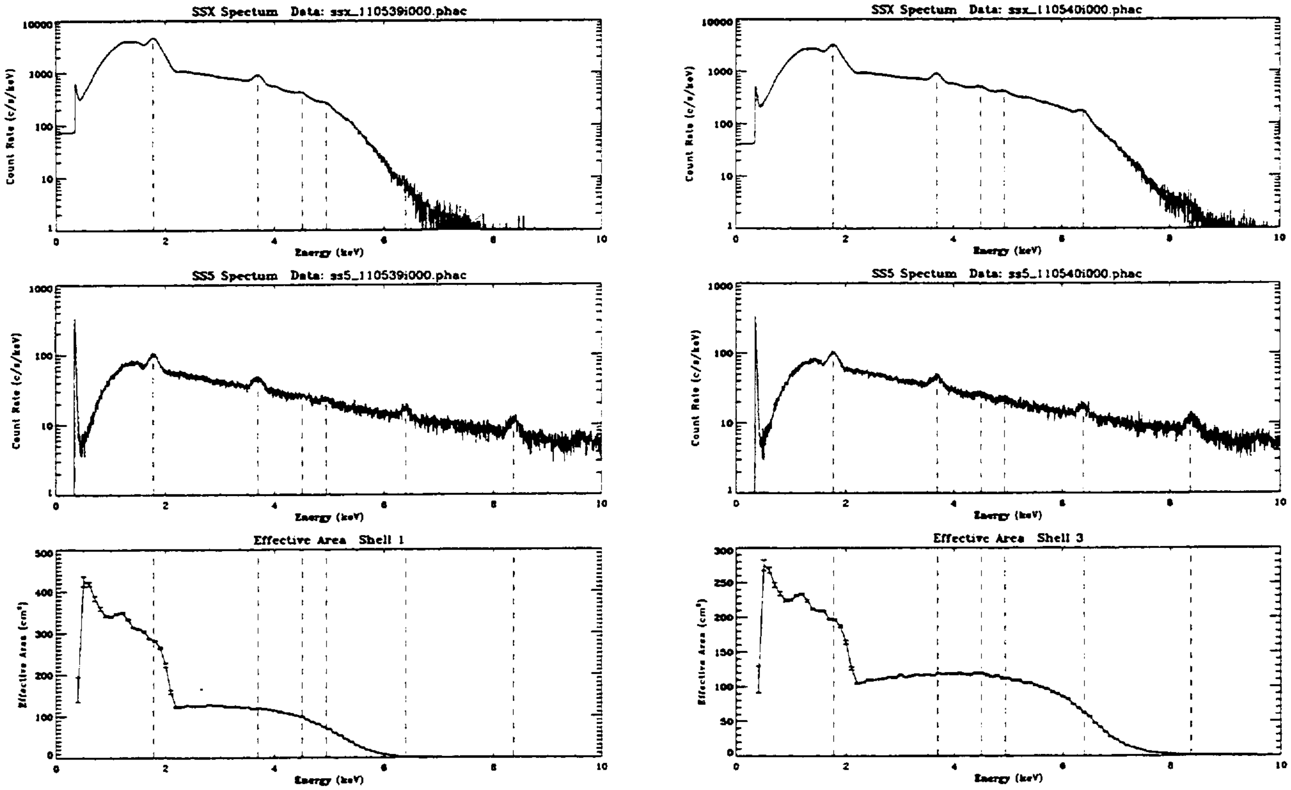

C-continuum effective area measurement: Shell 1.

C-continuum effective area measurement: Shell 3.

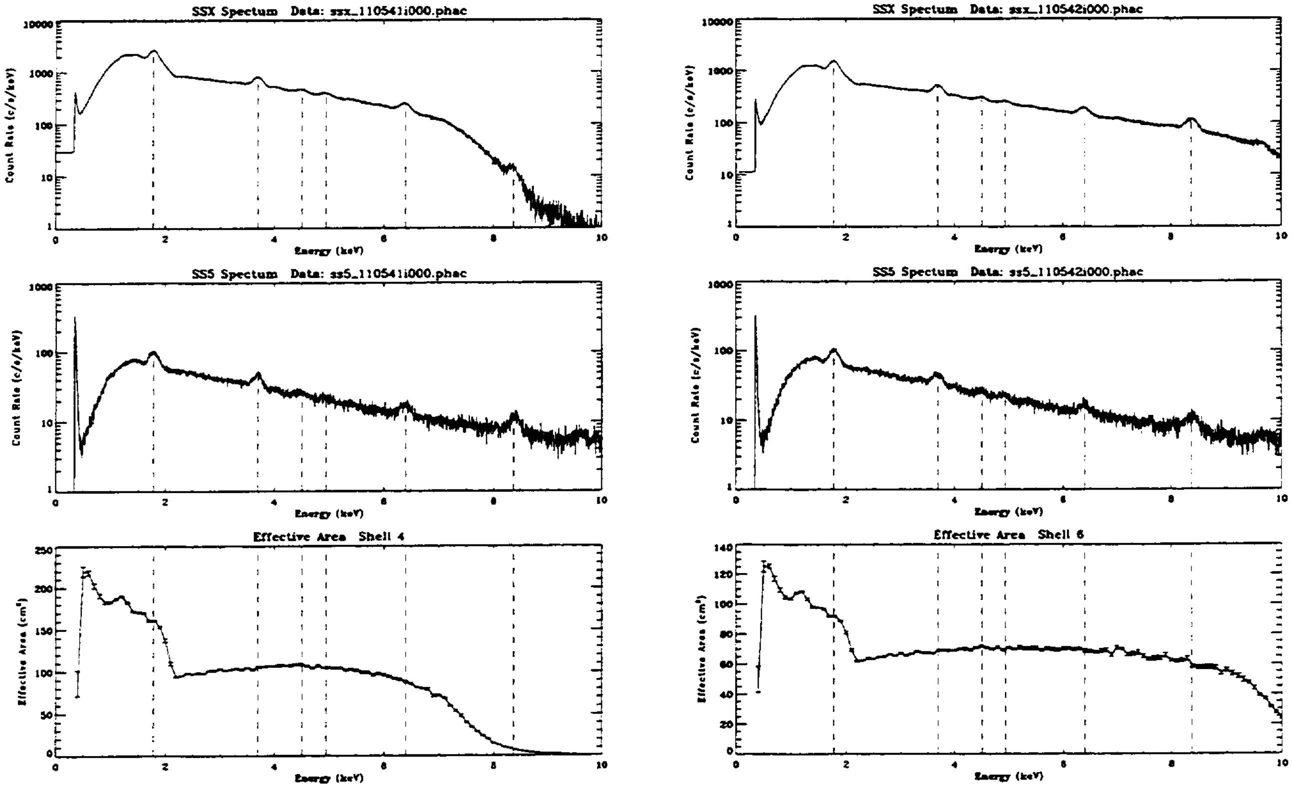

C-continuum effective area measurement: Shell 4.

C-continuum effective area measurement: Shell 6.

Figure 15: SSD C-continuum effective area measurements for the four shells: 2 mm aperture. Top panel of each quadrant plot is the SSX spectrum. Middle panel is the SS5 spectrum. Bottom panel is the measured effective area.

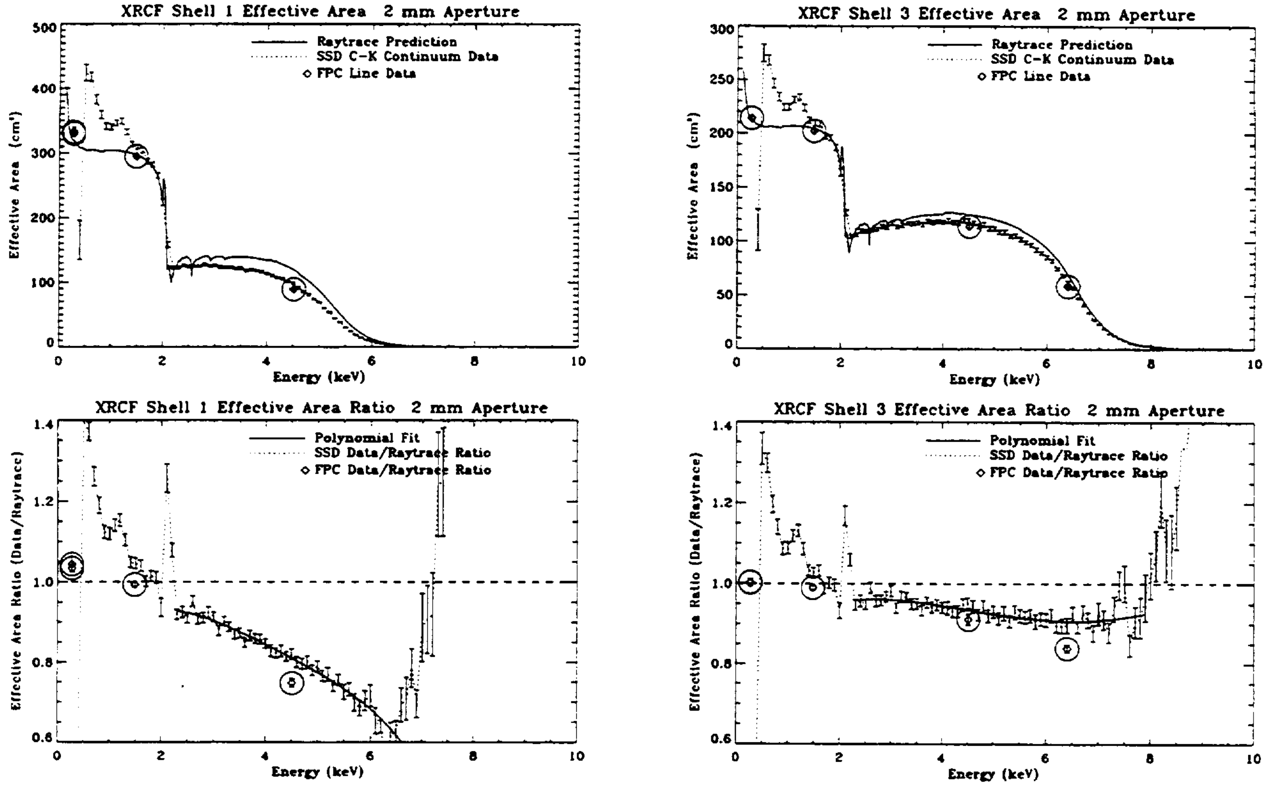

Calibration data vs. raytrace prediction: Shell 1. Calibration data vs. raytrace prediction: Shell 3.

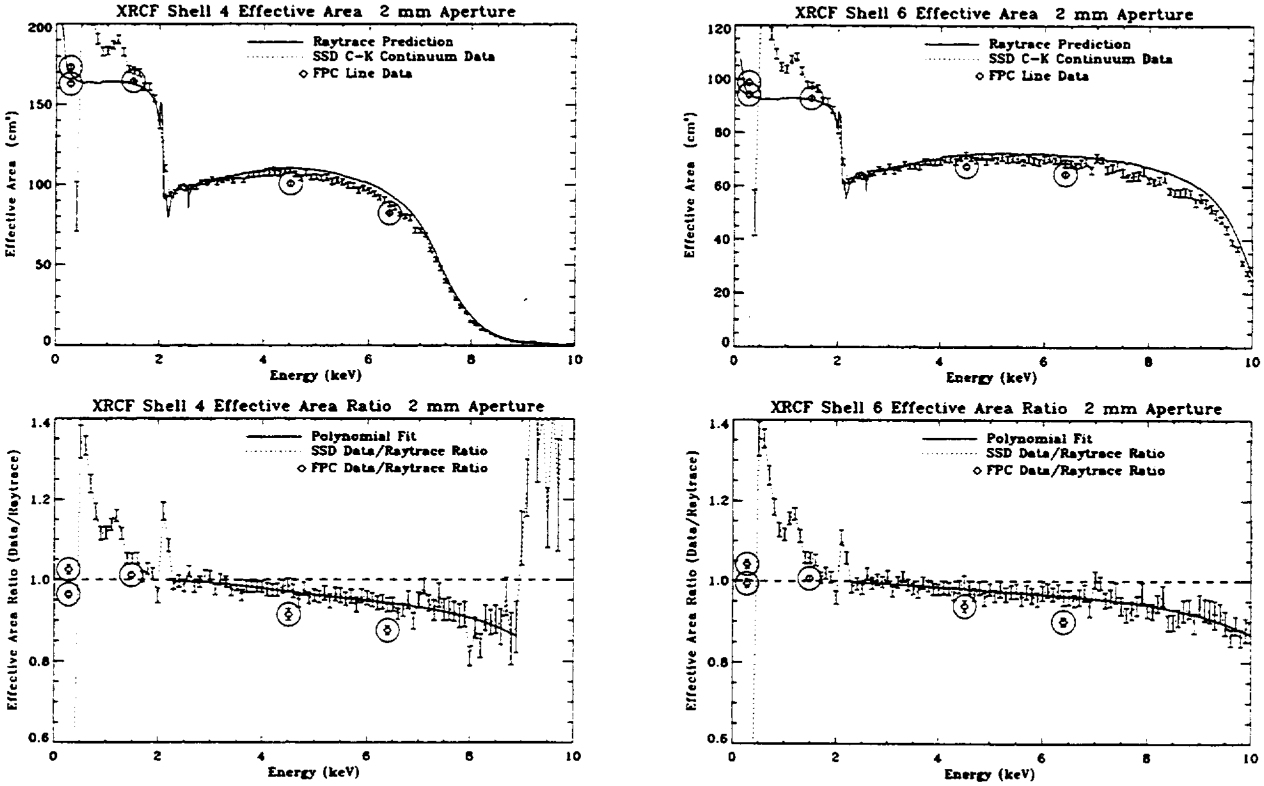

Calibration data vs. raytrace prediction: Shell 4. Calibration data vs. raytrace prediction: Shell 6.

Figure 16: Calibration data vs. raytrace prediction. Top panel of each quadrant plot shows the XRCF effective area within 2 mm aperture. Bottom panel shows the effective area ratio of data/raytrace.

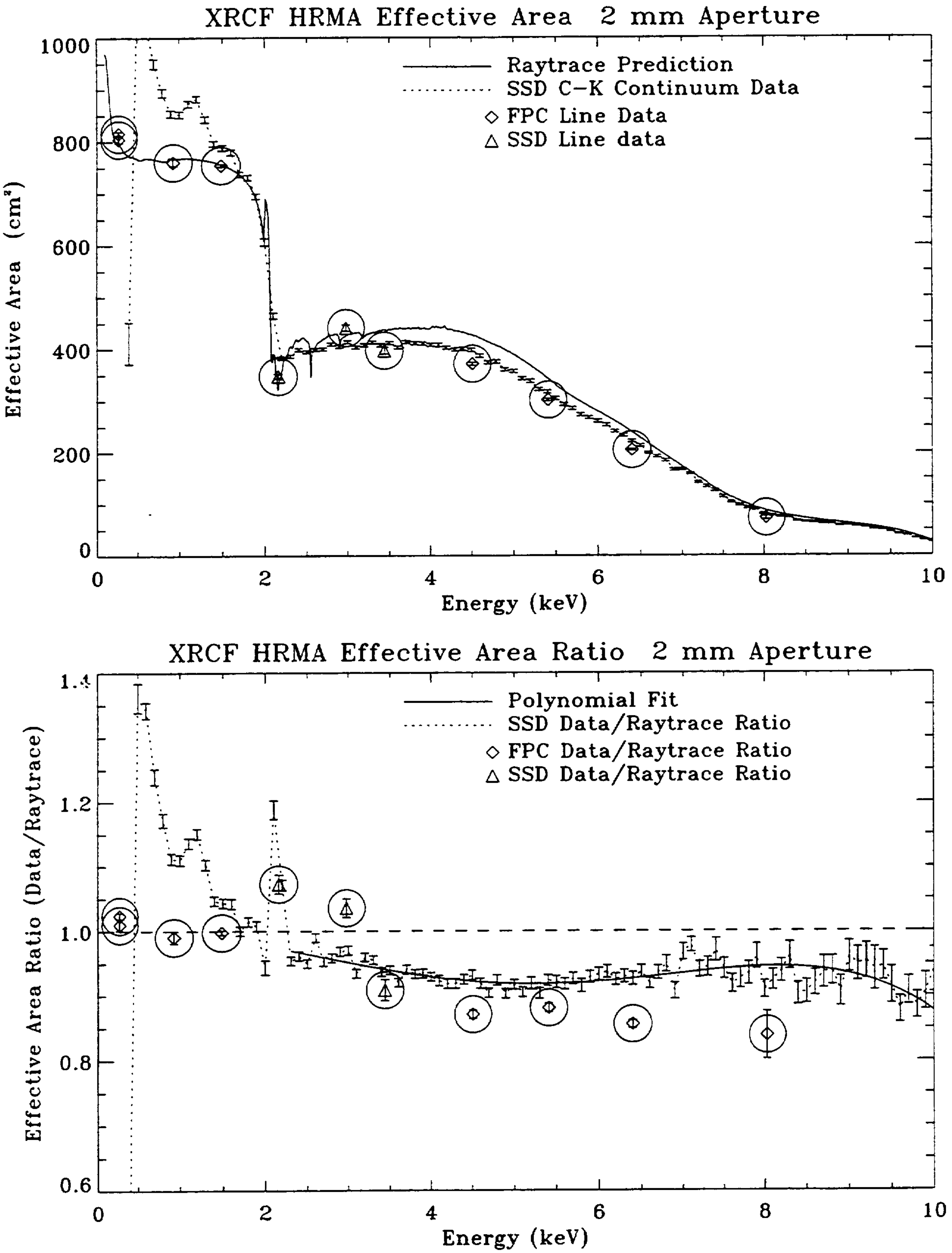

Figure 17: Calibration data vs. raytrace prediction. Top panel shows the XRCF HRMA effective area within 2 mm aperture. Bottom panel shows the effective area ratio of data/raytrace.

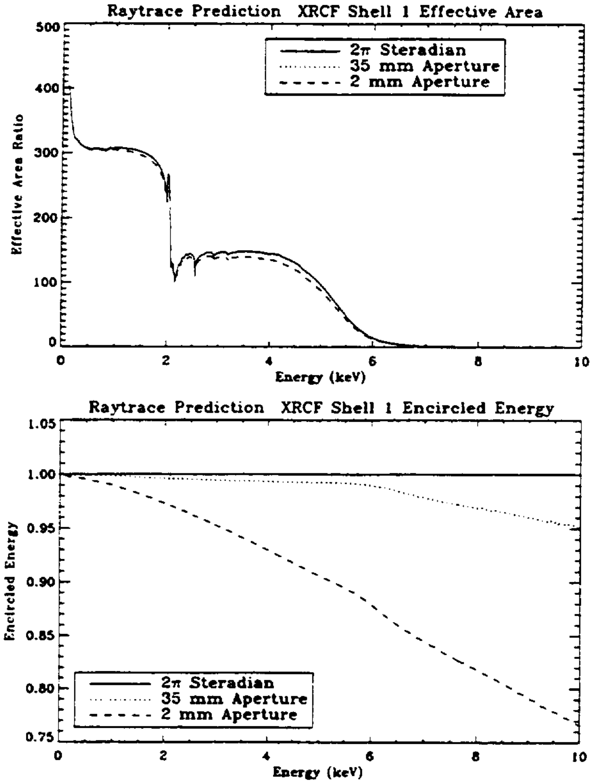

Figure 18: Raytrace prediction of XRCF Shell 1 effective area and encircled energy.

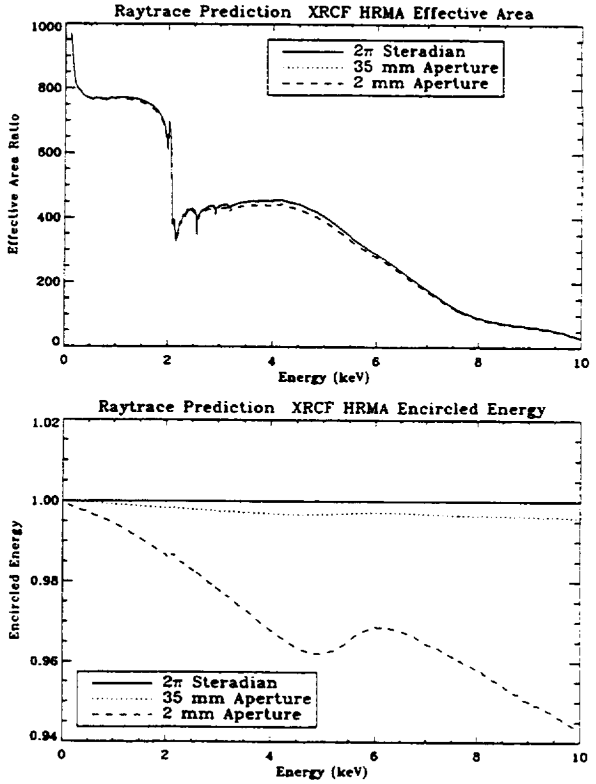

Figure 19: Raytrace prediction of XRCF HRMA effective area and encircled energy.

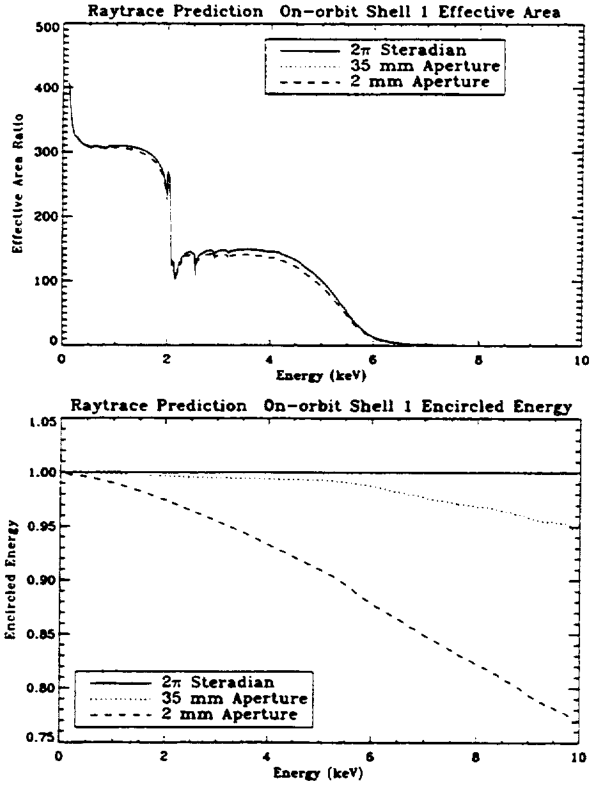

Figure 20: Raytrace prediction of on-orbit Shell 1 effective area and encircled energy.

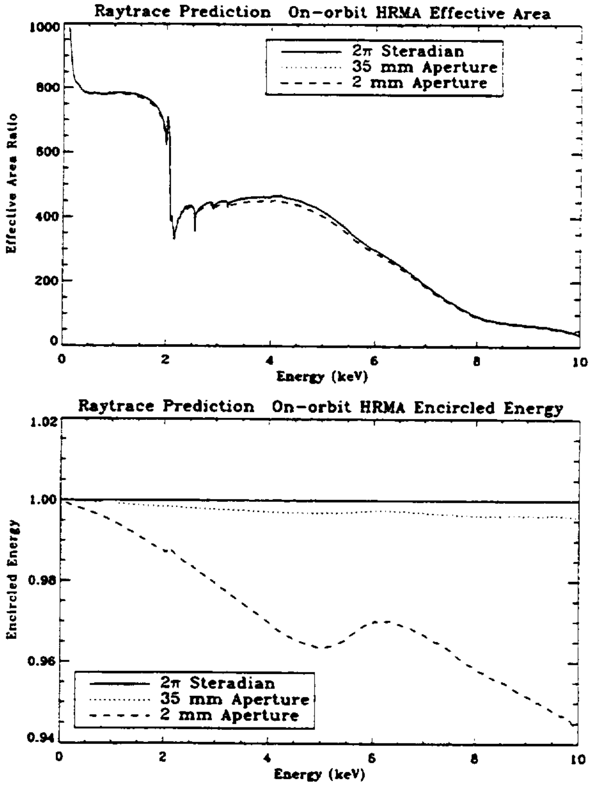

Figure 21: Raytrace prediction of on-orbit HRMA effective area and encircled energy.

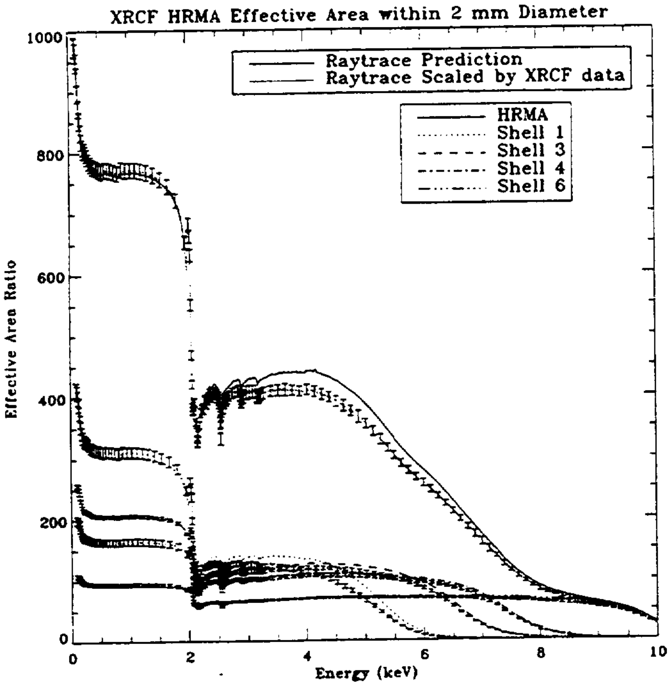

Figure 22: The XRCF HRMA and four shells effective areas within 2 mm aperture. Raytrace prediction scaled by the calibration data.

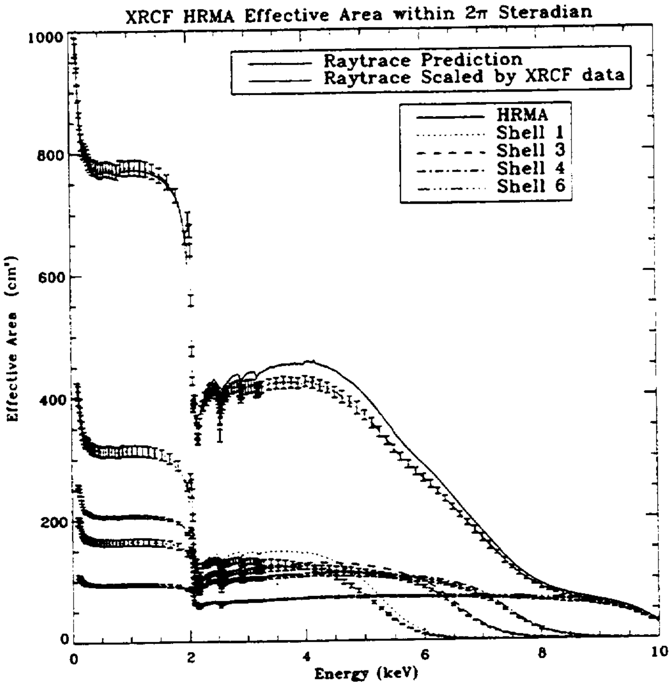

Figure 23: The XRCF HRMA and four shells effective areas within $2\pi$ steradian. Raytrace prediction scaled by the calibration data.

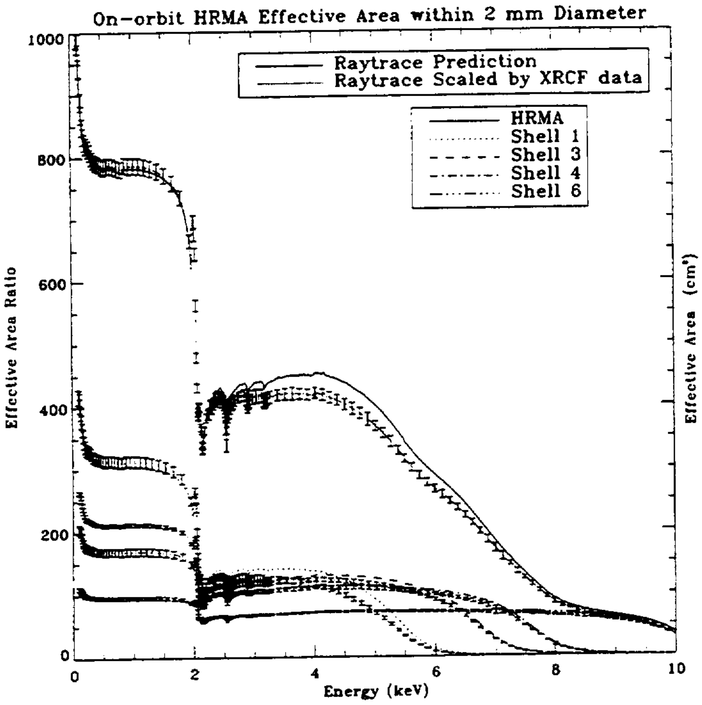

Figure 24: The on-orbit HRMA and four shells effective areas within 2 mm aperture. Raytrace prediction scaled by the calibration data.

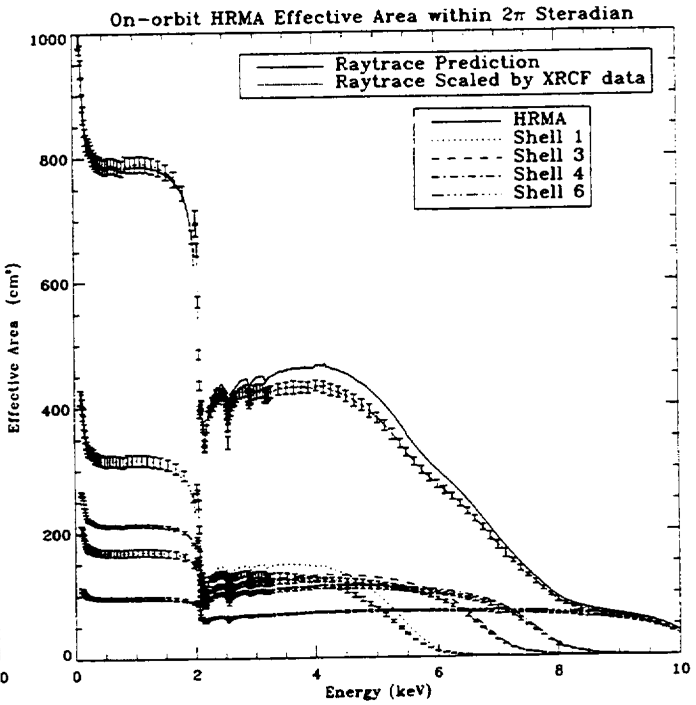

Figure 25: The on-orbit HRMA and four shells effective areas within $2\pi$ steradian. Raytrace prediction scaled by the calibration data.

# References

[1] J. J. Kolodziejczak, R. A. Austin, R. F. Elsner, S. L. O'Dell, M. E. Sulkanen, D. A. Swartz, A. F. Tennant, M. C. Weisskopf, G. Zirnstein, and W. C. McDermott, "Uses of continuum radiation on the AXAF calibration", *SPIE Proceedings* Vol. 3113, 65, San Diego, 1997.

[2] Ron Jenkins, R. W. Gould, and Dale Gedcke, "Quantitative X-Ray Spectrometry", *New York: Marcel Dekker, Inc.* 1981, pp. 266-267.

[3] Henke, L., Gullikson, E. M., and Davis, J. C. (1993). X-ray interactions: photoabsorpion, scattering, transmission, and reflection at E=50–30,000 eV, Z=1–92. *Atomic Data and Nuclear Data Tables*, 54:181. Additional data were taken from `http://www-cxro.lbl.gov/optical_constants/`.

[4] Graessle, D. E., Burek, A. J., Fitch, J. J., Harris, B., Schwartz, D. A., and Blake, R. L. "Optical constant from synchrotron reflectance measurements of AXAF witness mirrors 2 to 12 keV", *SPIE Proceedings*, Vol. 3113, 52, San Diego, 1997.

[5] Beckmann, P. and Spizzichino, A. (1963). *The Scattering of Electromagnetic Waves from Rough Surfaces.* Pergamon Press, Oxford.

# Appendix B

## Considerations of Projection Effects upon Determinations of Cosmological Parameters Using the Sunyaev Zel'dovich Effect.

**Center for Astrophysics**

Harvard College Observatory
Smithsonian Astrophysical Observatory

## MEMORANDUM

July 2, 1997

**To:** File

**From:** L. Van Speybroeck

**Subject:** Ellipticity and the Hubble Constant, rev a

## 1. Projection of ellipsoids [1]

Suppose that the volume emissivity is a function $G(\zeta)$, where:

$$\zeta = \frac{x_0^2 + y_0^2}{B_0^2} + \frac{z_0^2}{A_0^2}$$

where $x_0$, $y_0$, and $z_0$ are coordinates along the principal axes of the ellipsoid. We also suppose that the symmetry axis $z_0$ makes an angle $i$ with the $z$ axis, which is along the line of sight, and that the rotation is about the $y = y_0$ axis. Then, the projected surface brightness in the observing coordinate system will be given by:

$$\begin{aligned} I(x,y) &= \int_{-\infty}^{\infty} dz\, G(\zeta) \\ &= \frac{B_0}{R} \int_{\eta}^{\infty} d\zeta \, \frac{G(\zeta)}{(\zeta - \eta)^{\frac{1}{2}}} \qquad (1) \\ &= \frac{B_0}{R} F(\eta) \end{aligned}$$

---

[1] The work in this section comes from Fabricant, et. al., 1984 ApJ, 286, 186, and actually was brought to my attention as part of the work done by Alexey Vikhlinin.

where:

$$
\begin{aligned}
R &= \left(\frac{B_0^2}{A_0^2}\cos^2 i \; + \; \sin^2 i\right)^{\frac{1}{2}} \\
A &= RA_0 && \text{The observed semiaxis} \\
B &= B_0 && \text{The observed semiaxis} \\
\eta &= \frac{x^2}{A^2} + \frac{y^2}{B^2}
\end{aligned}
$$

A considerable amount of algebra goes into the above derivation; basically one expresses $\zeta$ in terms of the laboratory system (using $x_0 = x\cos i - z\sin i$, $z_0 = x\sin i + z\cos i$); finds, for a given pair $x, y$ the minimum value of $\zeta$ (by differentiating with respect to $z$), call this minimum value $\eta(x,y)$, solve for $z$ in terms of the quantity $\zeta - \eta$ (which is linear in $z$), calculates the derivative $dz/d\zeta = dz/d(\zeta - \eta)$, converts from an integral in $z$ to one in $\zeta$, and combines terms in the expressions for $dz/d\zeta$ and $\eta$.

## 2. X-ray and SZ projections for an isothermal gas [2]

The X-ray gas volume emissivity is proportional to a function of temperature $j(T)$ and the electron density squared. Using a $\beta$ model, one has:

$$\epsilon = \frac{n_0^2 j(T)}{(1+\zeta)^{3\beta}}$$

For the SZ effect, one has an equivalent gas volume emissivity:

$$Y = C\frac{n_0 T}{(1+\zeta)^{\frac{3\beta}{2}}}$$

where $C$ contains only well known constants.

and, using equation 1, one obtains:

$$I_X(x,y) = \frac{B_0}{R}\int_{\eta}^{\infty} d\zeta \, \frac{n_0^2 j(T)}{(1+\zeta)^{3\beta}(\zeta-\eta)^{\frac{1}{2}}} \qquad (2)$$

---

[2] Most of this work is similar to that done by Alexey Vikhlinin, and is similar to earlier treatments.

$$
\begin{aligned}
&= n_0^2 j(T) \frac{B_0}{R} F_1(\eta, \beta) && (3) \\
y(x,y) &= \frac{B_0}{R} C \int_\eta^\infty d\zeta \, \frac{n_0^2 j(T)}{(1+\zeta)^{\frac{3\beta}{2}} (\zeta - \eta)^{\frac{1}{2}}} && (4) \\
&= n_0 T \frac{B_0}{R} F_2(\eta, \beta) && (5) \\
& && (6)
\end{aligned}
$$

where:

$$
\begin{aligned}
F_1(\eta, \beta) &= (1+\eta)^{(\frac{1}{2} - 3\beta)} B(\frac{1}{2}, 3\beta - \frac{1}{2}) && (7) \\
F_2(\eta, \beta) &= (1+\eta)^{(\frac{1}{2} - \frac{3\beta}{2})} B(\frac{1}{2}, \frac{3\beta}{2} - \frac{1}{2}) && (8) \\
B(x,y) &= \frac{\Gamma(x)\Gamma(y)}{\Gamma(x+y)} && (9)
\end{aligned}
$$

The conversion of $I_X(x,y)$ to a surface brightness $\psi(\theta_x, \theta_y)$ requires a factor relating the angular size and luminosity distances, $d_A$ and $d_L$ respectively, which isn't interesting for this discussion , but is given by:

$$
\psi(\theta_x, \theta_y) = \frac{1}{4\pi} \left( \frac{d_A}{d_L} \right)^2 I_X(d_A\theta_x, d_A\theta_y) = \frac{1}{4\pi(1+z)^4} I_X(d_A\theta_x, d_A\theta_y)
$$

Combining the above equations in a manner to eliminate the electron density, one obtains:

$$
B_0 = \left[ \left( \frac{y(\theta_x, \theta_y)}{CT} \right)^2 \frac{j(T)}{4\pi\psi(\theta_x, \theta_y)} \frac{F_1(\eta, \beta)}{((1+z)^2 F_2(\eta, \beta))^2} \right] R \qquad (10)
$$

The bracketed quantities all can be measured or calculated, but the scale factor $R$ cannot be measured, and so it is necessary to make repeated measurements and work from the distribution of R.

The Hubble constant is obtained from:

$$
B_0 = d_A \Theta_B = \frac{c}{H_0} f(z, \Omega_0, \lambda) \qquad (11)
$$

Where $\Theta_B$ is the measurable angle corresponding to $B_0$, $z$ is the redshift, $\Omega_0$ is the mass density curvature term, and $\lambda$ is the cosmological constant (if any).

Thus, for the purposes of this discussion, we can write:

$$H_0 = K\frac{\Theta_B}{R} \tag{12}$$

Where $K$ combines quantities which are known or can be measured. $\Theta_B$ also can be measured, but a possible error is to confuse $\Theta_B$ with the scale angle $\Theta_A$ along the other axis (ie, assuming that the basic cluster is prolate, when it actually is oblate, or the reverse), and so we keep it separate to facilitate the discussion below.

We will not be able to evaluate the quantity $R$ in the measurement process, and so we will have to define some other function of the observables. Let us define a measurement by:

$$H_0^{(i)} = Kh_i(\Theta_A, \Theta_B) \tag{13}$$

and the corresponding value which is obtained when we confuse the two axes:

$$H_m^{(i)} = Kh_i(\Theta_B, \Theta_A) \tag{14}$$

We will discuss the distributions of the measured quantities below in terms of their ratio to the correct values, so we will be interested in the distributions of:

$$\frac{H_0^{(i)}}{H_0} = \frac{h_i(\Theta_A, \Theta_B)R}{\Theta_B} \tag{15}$$

and:

$$\frac{H_m^{(i)}}{H_0} = \frac{h_i(\Theta_B, \Theta_A)R}{\Theta_B} \tag{16}$$

## 3. Distribution of projected quantities [3]

---

[3] The work in this section is similar to that done by Alexey Vikhlinin, but contains some extensions.

The quantity $\cos i$ is uniformly distributed on the interval $(-1, 1)$ if clusters are oriented randomly, and so distributions of functions which depend only on $\cos i$ take on a particularly simple form. Let us suppose that we are considering the distribution of a function $f(\cos i)$; if the function is monotonic from $\cos i = -1$ to $\cos i = 1$, then the probability that the function will yield a value between $f(\cos \phi_1)$ and $f(\cos \phi_2)$ is just $|\cos \phi_1 - \cos \phi_2|/2$, and the extremes of the function are $f(-1)$ and $f(1)$. If, on the other hand, the function is symmetric about $\cos i = 0$, then the probability that the function will yield a value between $f(\cos \phi_1)$ and $f(\cos \phi_2)$ is just $|\cos \phi_1 - \cos \phi_2|$, where $\cos \phi_1$ and $\cos \phi_2$ are limited to non-negative values, and the extremes of the function are given by $f(0)$ and $f(1)$. More complex functions could be divided into additional monotonic intervals, but this will not be required for our analysis here. Formally, if the cumulative probability distribution is $P(f)$, then we write:

$$|P(f(\cos \phi_2)) - P(f(\cos \phi_1))| \;=\; |\cos \phi_2 - \cos \phi_1|/\mu \tag{17}$$

where $\mu$ is 2 if $f(\cos \phi)$ in monotonic on the interval $(-1, 1)$, and $\mu$ is 1 if $f(\cos \phi)$ is symmetric in its argument and monotonic on the interval $(0, 1)$; in the latter case we also limit $\cos \phi$ to this interval.

The average value of $f(\cos i)$ is simply given by:

$$\mu \langle f \rangle \;=\; \int_{1-\mu}^{1} d\cos i \, f(\cos i) \tag{18}$$

where the lower limit to the integral is just an irritating way to write 0 or $-1$.

The differential probability density is given by:

$$\mu \frac{dP(v)}{dv} \;=\; \pm \frac{d}{dv} f^{-1}(v) \;=\; \pm \left( \frac{d}{d\cos i} f(\cos i) \right)^{-1} \Bigg|_{f(\cos i)=v} \tag{19}$$

(where $v = f(\cos i)$, and the $\pm$ sign is determined by whether the function is monotonically increasing or decreasing in the interval.

If the function depends upon $\cos i$ as described above, but also depends upon some other set of parameters $\alpha$ which have a probability density $\rho(\alpha)$, then the differential probability density will be given by:

$$\mu\frac{dP(v)}{dv} = \pm\int d\alpha\,\rho(\alpha)\frac{d}{dv}f^{-1}(v,\alpha) = \pm\int d\alpha\,\rho(\alpha)\left(\frac{d}{d\cos i}f(\cos i,\alpha)\right)^{-1}\Bigg|_{f(\cos i)=v} \tag{20}$$

In the discussion below, we will be concerned primarily with the *median* of a set of measurements, and so it is worth considering how the median is distributed. This may not be the optimum estimator, but there certainly is no need to do *worse*. For the sake of simplicity, we limit ourselves to an odd number of measurements, say $(2n+1)$, and we suppose that the interval is $(-1,1)$. Then, the distribution of the median of function of a set of measurements of a uniformly distributed variable $x$ is given by:

$$\frac{d}{dx}P(x,n) = N(x+1)^n(1-x)^n = N(1-x^2)^n \tag{21}$$

Where $N$ is a normalization constant. The probability that the median $x_m$ will lie in the interval $-x, x$ thus is:

$$P(-x < x_m < x, n) = \frac{\int_0^x dx\,(1-x^2)^n}{\int_0^1 dx\,(1-x^2)^n} \tag{22}$$

$$= \frac{2\Gamma(\frac{3}{2}+n)}{\sqrt{\pi}n!}\,{}_2\mathrm{F}_1(\frac{1}{2},-n;\frac{3}{2};x^2)\,x \tag{23}$$

The confidence intervals for functions symmetric about $\cos i = 0$ will be centered on $\cos i = 1/2$, and will be half as large as the ones given by equation 22. Some values:

| Data Points | Interval = $(-1,1)$<br>$x:\ P(-x < x_m < x) =$ | | | Interval = $(0,1)$<br>$x:\ P(\frac{1}{2} - x < x_m < \frac{1}{2} + x) =$ | | |
|---|---|---|---|---|---|---|
| $2n+1$ | 0.683 | 0.900 | 0.950 | 0.683 | 0.900 | 0.950 |
| 3 | 0.496 | 0.729 | 0.811 | 0.248 | 0.365 | 0.406 |
| 5 | 0.407 | 0.621 | 0.707 | 0.203 | 0.311 | 0.353 |
| 7 | 0.353 | 0.549 | 0.632 | 0.177 | 0.275 | 0.316 |
| 9 | 0.316 | 0.497 | 0.576 | 0.158 | 0.249 | 0.288 |
| 11 | 0.288 | 0.458 | 0.532 | 0.144 | 0.229 | 0.266 |
| 13 | 0.267 | 0.426 | 0.497 | 0.134 | 0.213 | 0.249 |
| 15 | 0.250 | 0.400 | 0.468 | 0.125 | 0.200 | 0.234 |
| 17 | 0.236 | 0.378 | 0.444 | 0.118 | 0.189 | 0.222 |
| 19 | 0.224 | 0.360 | 0.423 | 0.112 | 0.180 | 0.211 |
| 21 | 0.213 | 0.344 | 0.404 | 0.107 | 0.172 | 0.202 |
| 23 | 0.204 | 0.330 | 0.388 | 0.102 | 0.165 | 0.194 |
| 25 | 0.196 | 0.317 | 0.374 | 0.098 | 0.159 | 0.187 |
| 27 | 0.189 | 0.306 | 0.361 | 0.095 | 0.153 | 0.181 |
| 29 | 0.183 | 0.296 | 0.349 | 0.091 | 0.148 | 0.175 |
| 31 | 0.177 | 0.287 | 0.339 | 0.088 | 0.143 | 0.169 |

## 4. Examples of distributions of estimators

In this section we will let $r_0 = B_0/A_0$ be the ratio of the intrinsic semimajor axes of the cluster, and we will give examples for various values of $r_0$. Actually, of course, clusters require at least a distribution of the values of $r_0$. Typical medians of observed ellipticities are of order 0.25; if this distribution resulted from the various projections of a single axial ratio $r_0$, then the value of $r_0$ would be about 0.7 if the clusters are prolate, and about 1.55 if the clusters are oblate. We will use values like these in this range below.

### 4.1. Example 1, assume $R = 1$; $h_1(\Theta_A, \Theta_B) = \Theta_B$

In this case, the distribution of the quantity

$$\frac{H_0^{(1)}}{H_0} = R(r_0, \cos i) \tag{24}$$

is required. The distribution is shown for prolate spheroids in figure 1 and for oblate spheroids in figure 2. The 5%, 50%, and 95% points of the distributions are given in table 1. We see that there is an expected error in the median of order 7% for the more likely prolate shape, and a somewhat larger error for the oblate shapes. The expected errors have a significant dependence upon the underlying and unmeasurable intrinsic ratio of the semimajor axes. The 90% confidence interval, normalized for the bias at $r_0 = 0.7$, is about 16% full width. The sensitivity to the intrinsic ratio of the semimajor axes would add another uncertainty of order 10%.

The expected average of the measurements is:

$$\begin{aligned}
\left\langle \frac{H_0^{(1)}}{H_0} \right\rangle &= \frac{1}{2}\left( r_0 + \frac{\arcsin(\sqrt{1 - r_0^2})}{\sqrt{1 - r_0^2}} \right) && \text{Prolate}; r_o < 1 \\
&= \frac{1}{2}\left( r_0 + \frac{\operatorname{arcsinh}(\sqrt{r_0^2 - 1})}{\sqrt{r_0^2 - 1}} \right) && \text{Oblate}; r_o > 1
\end{aligned}$$

In this case we also must consider the possibility that we will erroneously assign the axes. In this case, the distribution of the quantity

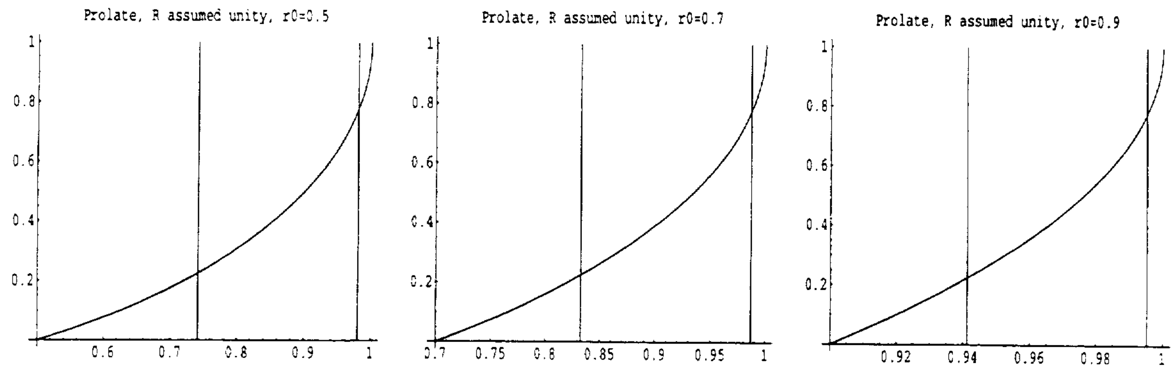

Figure 1: Cumulative distributions of the ratio of the measured value of $H_0$ to the true value for prolate spheroids using the estimator $h_1(\Theta_A, \Theta_B) = \Theta_B$. The 5% to 95% confidence interval for the median of 7 data points is indicated.

Table 1: Percentage points for median of 7 points, $h_1(\Theta_A, \Theta_B) = \Theta_B$

| $r_0$ | Percentage Points | | |
|---|---|---|---|
| | 5%, | 50% | 95% |
| 0.50 | 0.741 | 0.901 | 0.981 |
| 0.70 | 0.833 | 0.934 | 0.987 |
| 0.90 | 0.941 | 0.976 | 0.995 |
| 1.25 | 1.014 | 1.068 | 1.157 |
| 1.50 | 1.031 | 1.146 | 1.323 |
| 1.75 | 1.051 | 1.231 | 1.496 |

$$\frac{H_m^{(1)}}{H_0} = (R(r_0, \cos i))^2 / r_0 \tag{25}$$

is required. The distribution is shown for oblate spheroids mistaken as prolate in figure 3 and for prolate spheroids mistaken as oblate in figure 4. The 5%, 50%, and 95% points of the distributions are given in table 2. We see that there is a somewhat compensating effect, in that the bias corrections are of the same sense even if clusters actually are oblate, but we assume them to be prolate. The effect in this case is to add an additional error of order 6%. The effect of assuming that clusters are oblate, when they actually are prolate, is considerably worse, but we are not likely to make that error.

In this case the expected average of the measurement is given by:

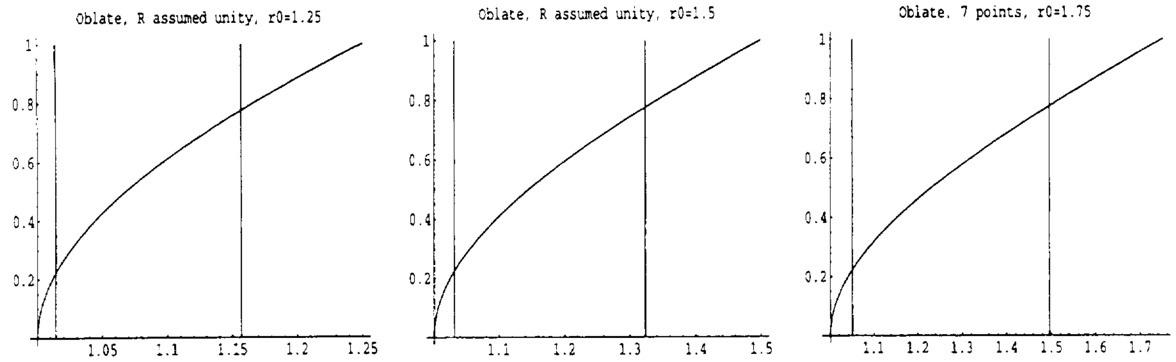

Figure 2: Cumulative distributions of the ratio of the measured value of $H_0$ to the true value for oblate spheroids using the estimator $h_1(\Theta_A, \Theta_B) = \Theta_B$. The 5% to 95% confidence interval for the median of 7 data points is indicated.

$$\left\langle \frac{H_0^{(1)}}{H_0} \right\rangle = \frac{2}{3r_0} + \frac{r_0}{3}$$

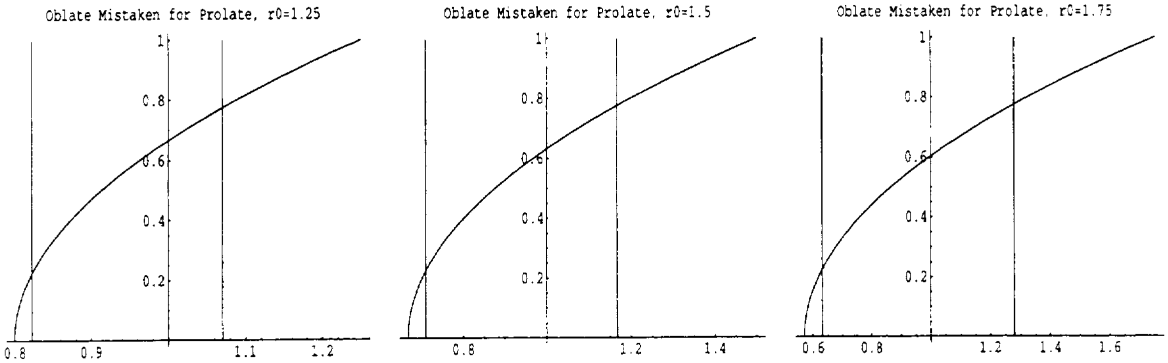

Figure 3: Cumulative distributions of the ratio of the measured value of $H_0$ to the true value for oblate spheroids using the erroneous estimator $h_1(\Theta_B, \Theta_A) = \Theta_A$. The 5% to 95% confidence interval for the median of 7 data points is indicated.

### 4.2. Example 2; $h_1(\Theta_A, \Theta_B) = \Theta_A^k \Theta_B^{1-k}$, $k = 0.25$

This is an attempt to partially compensate for the unobservable $R$ by correlating the results with the measured ellipticity. I investigated a number of powers and found $k \sim 0.25$ to be the most attractive.

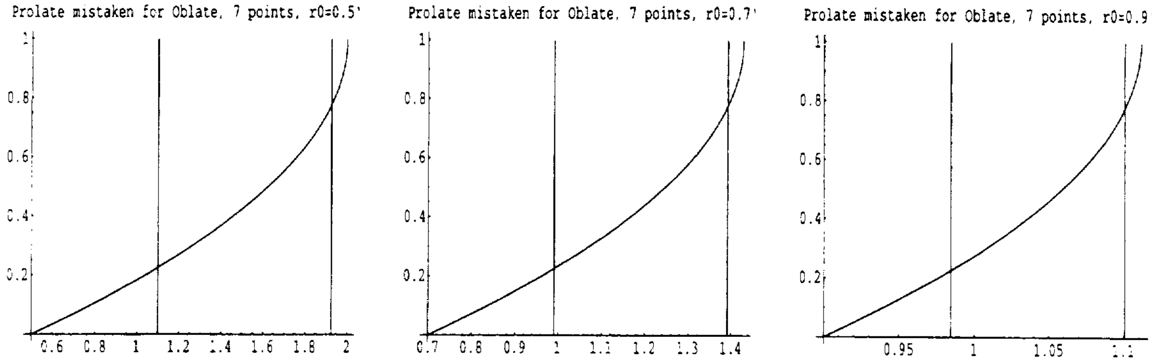

Figure 4: Cumulative distributions of the ratio of the measured value of $H_0$ to the true value for prolate spheroids using the erroneous estimator $h_1(\Theta_B, \Theta_A) = \Theta_A$. The 5% to 95% confidence interval for the median of 7 data points is indicated.

Table 2: Percentage points for median of 7 points with error in identification of axes, $h_1(\Theta_B, \Theta_A) = \Theta_A$

| $r_0$ | Percentage Points | | |
|---|---|---|---|
| | 5%, | 50% | 95% |
| 0.50 | 1.099 | 1.625 | 1.924 |
| 0.70 | 0.991 | 1.246 | 1.392 |
| 0.90 | 0.984 | 1.058 | 1.100 |
| 1.25 | 0.823 | 0.913 | 1.070 |
| 1.50 | 0.709 | 0.875 | 1.167 |
| 1.75 | 0.631 | 0.866 | 1.279 |

In this case, the distribution of the quantity

$$\frac{H_0^{(2)}}{H_0} = (R(r_0, \cos i))^{1+k} r_0^{-k} \tag{26}$$

is required. The distribution is shown for prolate spheroids in figure 5 and for oblate spheroids in figure 6. The 5%, 50%, and 95% points of the distributions are given in table 3 We see that the expected bias in the median is small for the prolate or slightly oblate cases, and is relatively insensitive to the underlying and unmeasurable intrinsic ratio of the semimajor axes. The 90% confidence interval, normalized for the bias at $r_0 = 0.7$, is about 21% full width. The consequences of fewer and additional data points are explored in table 4, in which examples are given for 3 and 11 data points. We see that there is not a fast improvement between 3 and 11 for reasonably small values of the ellipticity.

The expected average of the measurements is:

$$\left\langle \frac{H_0^{(2)}}{H_0} \right\rangle = {}_2F_1\left(\frac{1}{2}, \frac{-(1+k)}{2}; \frac{3}{2}; 1 - r_0^2\right) r_0^{-k}$$

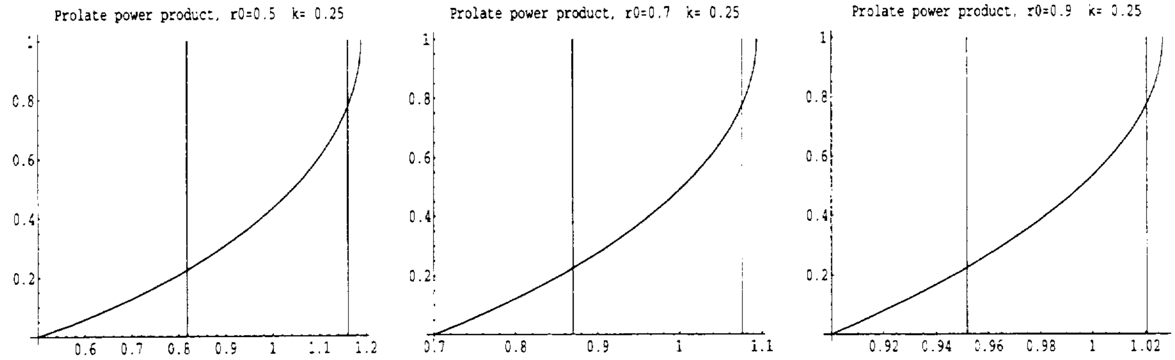

Figure 5: Cumulative distributions of the ratio of the measured value of $H_0$ to the true value for prolate spheroids using the estimator $h_1(\Theta_A, \Theta_B) = \Theta_A^{0.25}\Theta_B^{0.75}$. The 5% to 95% confidence interval for the median of 7 data points is indicated.

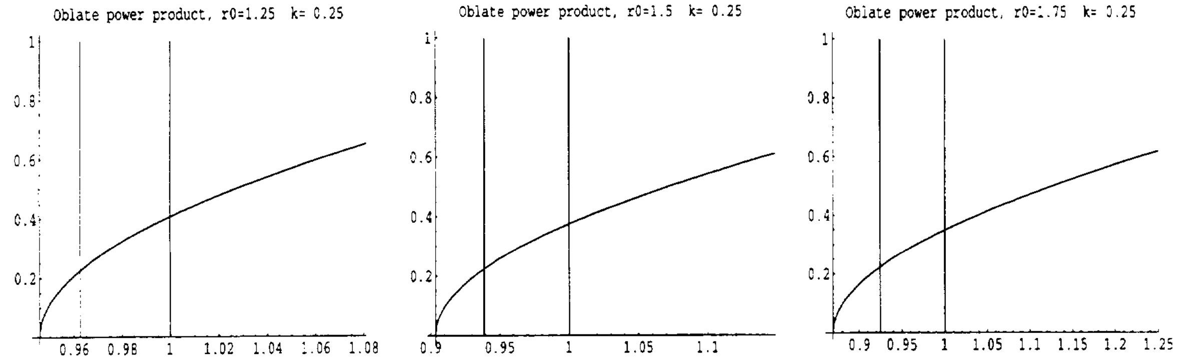

Figure 6: Cumulative distributions of the ratio of the measured value of $H_0$ to the true value for oblate spheroids using the estimator $h_1(\Theta_A, \Theta_B) = \Theta_A^{0.25}\Theta_B^{0.75}$. The 5% to 95% confidence interval for the median of 7 data points is indicated.

In this case we also must consider the possibility that we will erroneously assign the axes. In this case, the algebra is the same as for the correct identification, but with the substitution $k \rightarrow 1 - k$. Thus,

Table 3: Percentage points for median of 7 points, $h_1(\Theta_A, \Theta_B) = \Theta_A^{0.25}\Theta_B^{0.75}$

| $r_0$ | Percentage Points | | |
|---|---|---|---|
| | 5%, | 50% | 95% |
| 0.50 | 0.818 | 1.045 | 1.161 |
| 0.60 | 0.839 | 1.019 | 1.113 |
| 0.70 | 0.870 | 1.004 | 1.076 |
| 0.75 | 0.888 | 1.000 | 1.060 |
| 0.80 | 0.908 | 0.997 | 1.045 |
| 0.85 | 0.929 | 0.996 | 1.032 |
| 0.90 | 0.952 | 0.996 | 1.021 |
| 1.25 | 0.962 | 1.027 | 1.134 |
| 1.50 | 0.939 | 1.071 | 1.282 |
| 1.75 | 0.925 | 1.127 | 1.439 |

$$\frac{H_m^{(2)}}{H_0} = \left(R(r_0, \cos i)\right)^{2-k} r_0^{k-1} \tag{27}$$

The distribution is shown for oblate spheroids mistaken as prolate in figure 7 and for prolate spheroids mistaken as oblate in figure 8. The 5%, 50%, and 95% points of the distributions are given in table 5. Again, the penalty for a mis-identification of the axes is about 6%.

In this case the expected average of the measurement is given by:

$$\left\langle \frac{H_m^{(2)}}{H_0} \right\rangle = {}_2\mathrm{F}_1(\frac{1}{2}, \frac{-(2-k)}{2}; \frac{3}{2}; 1 - r_0^2) r_0^{k-1}$$

### 4.3. Example 3; $h_1(\Theta_A, \Theta_B) = \Theta_A^k \Theta_B^{1-k}$, $k = 0.5$

This also is an attempt to partially compensate for the unobservable $R$ by correlating the results with the measured ellipticity, but in a manner insensitive to the identification of the axes.

The distribution is shown for prolate spheroids in figure 9 and for oblate spheroids in figure 10. The 5%, 50%, and 95% points of the distributions are given in table 6 This estimator results in an over-estimate of $H_0$ for the more likely prolate case, and also a

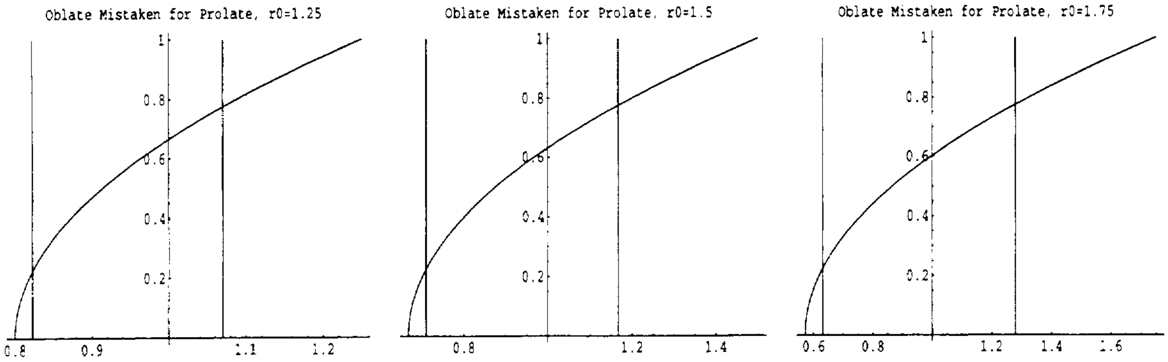

Figure 7: Cumulative distributions of the ratio of the measured value of $H_0$ to the true value for oblate spheroids using the erroneous estimator $h_1(\Theta_B, \Theta_A) = \Theta_A^{0.75}\Theta_B^{0.25}$. The 5% to 95% confidence interval for the median of 7 data points is indicated.

sensitivity to the underlying distribution of the ratios of semimajor axes. The behavior for oblate spheroids is more favorable, but unfortunately, this is a less likely case. The 90% confidence range for 7 points at $r_0 = 0.7$, normalized by the mean bias, has a 24% full width.

The expected average of the measurements is:

$$\left\langle \frac{H_0^{(2)}}{H_0} \right\rangle = {}_2\mathrm{F}_1(\frac{1}{2}, \frac{-3}{4}; \frac{3}{2}; 1 - r_0^2)\left(\frac{1}{\sqrt{r_0}}\right)$$

### 4.4. Example 4; $h_1(\Theta_A, \Theta_B) = \left(\frac{\Theta_A^k + \Theta_B^k}{2}\right)^{\frac{1}{k}}, k = 0.5$

This also is an attempt to partially compensate for the unobservable $R$ by correlating the results with the measured ellipticity, but in a manner insensitive to the identification of the axes.

The distribution is shown for prolate spheroids in figure 11 and for oblate spheroids in figure 12. The 5%, 50%, and 95% points of the distributions are given in table 7. This estimator results in an over-estimate of $H_0$ for the more likely prolate case, and also a sensitivity to the underlying distribution of the ratios of semimajor axes. The behavior for oblate spheroids is more favorable, but unfortunately, this is a less likely case. The 90% confidence range for 7 points at $r_0 = 0.7$, normalized by the mean bias, has a 25% full width.

### 4.5. Example 5; $h_1(\Theta_A, \Theta_B) = \left(\frac{\Theta_A + \Theta_B}{2}\right)$

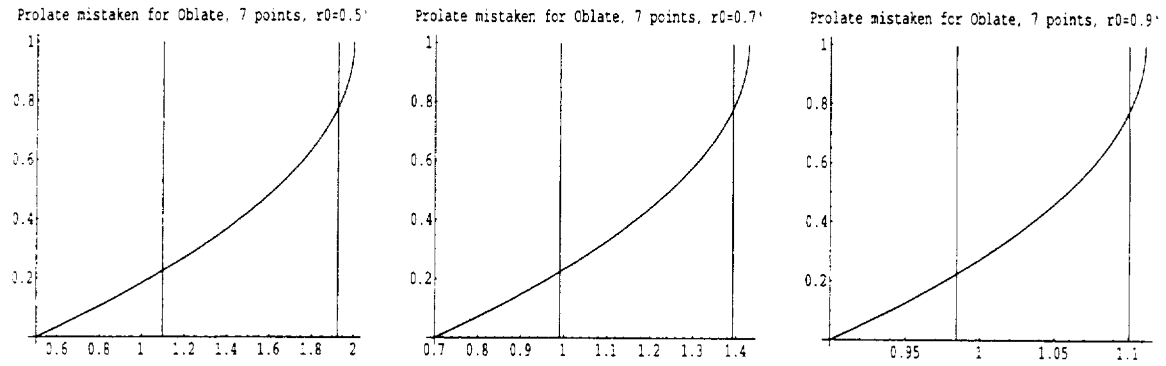

Figure 8: Cumulative distributions of the ratio of the measured value of $H_0$ to the true value for prolate spheroids using the erroneous estimator $h_1(\Theta_B, \Theta_A) = \Theta_A^{0.75}\Theta_B^{0.25}$. The 5% to 95% confidence interval for the median of 7 data points is indicated.

This also is an attempt to partially compensate for the unobservable $R$ by correlating the results with the measured ellipticity, but in a manner insensitive to the identification of the axes.

The distribution is shown for prolate spheroids in figure 13 and for oblate spheroids in figure 14. The 5%, 50%, and 95% points of the distributions are given in table 8. This estimator results in an over-estimate of $H_0$ for the more likely prolate case, and also a sensitivity to the underlying distribution of the ratios of semimajor axes. The behavior for oblate spheroids is more favorable, but unfortunately, this is a less likely case. The 90% confidence range for 7 points at $r_0 = 0.7$, normalized by the mean bias, has a 25% full width.

## 5. Conclusion

From the cases studied here, I prefer the estimator $h_1(\Theta_A, \Theta_B) = \Theta_A^{0.25}\Theta_B^{0.75}$), because it is relatively insensitive to the intrinsic ratio of semimajor axes, and therefore probably insensitive to the distribution of this quantity.

The uncertainty in the result would be significantly reduced if we can select clusters which may be nearly spherical. There is some evidence (Wang and Ulmer, obtained from the web; http://xxx.lanl.gov.archive.astro-ph) that clusters which are deficient in blue galaxies also are rounder, and of course we can select for absence of structure in ROSAT or the radio data where it exists.

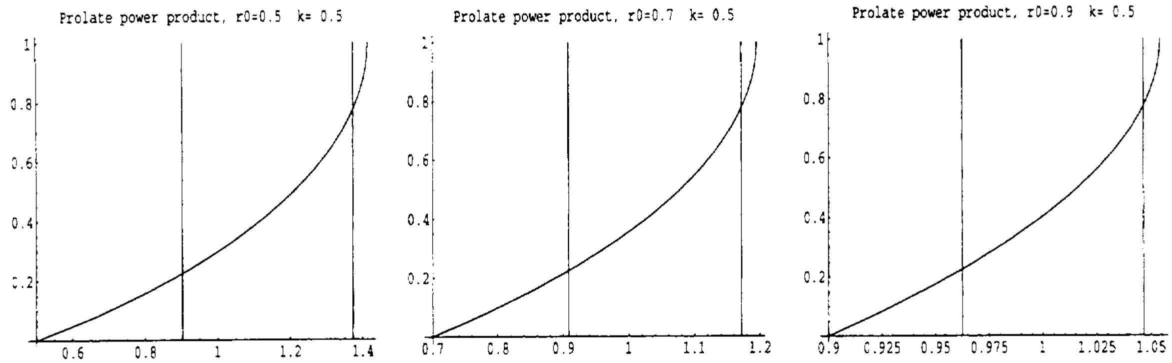

Figure 9: Cumulative distributions of the ratio of the measured value of $H_0$ to the true value for prolate spheroids using the estimator $h_1(\Theta_A, \Theta_B) = \Theta_A^{0.5}\Theta_B^{0.5}$. The 5% to 95% confidence interval for the median of 7 data points is indicated.

Of course, the main selection must be based upon temperature and luminosity.

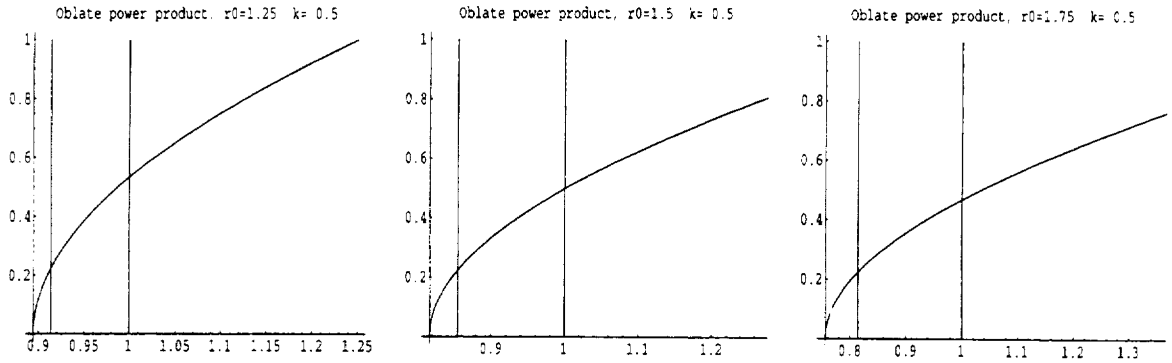

Figure 10: Cumulative distributions of the ratio of the measured value of $H_0$ to the true value for oblate spheroids using the estimator $h_1(\Theta_A, \Theta_B) = \Theta_A^{0.5}\Theta_B^{0.5}$. The 5% to 95% confidence interval for the median of 7 data points is indicated.

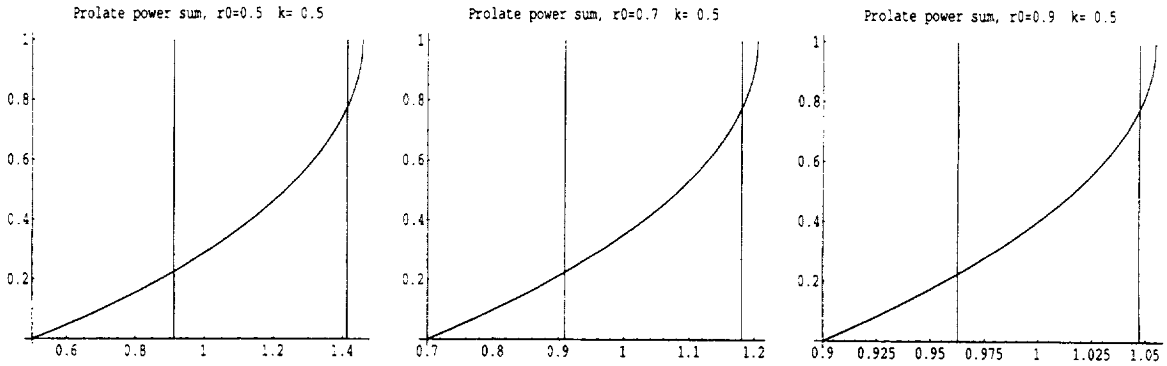

Figure 11: Cumulative distributions of the ratio of the measured value of $H_0$ to the true value for prolate spheroids using the estimator $h_1(\Theta_A, \Theta_B) = [(\Theta_A^{0.5} + \Theta_B^{0.5})/2]^2$. The 5% to 95% confidence interval for the median of 7 data points is indicated.

Table 4: Percentage points for median of 3 to 31 points, $h_1(\Theta_A, \Theta_B) = \Theta_A^{0.25}\Theta_B^{0.75}$

| $r_0$ | 50% | 5%, 16%, 84%, and 95% points for N data points, N= | | | | | | | |
|---|---|---|---|---|---|---|---|---|---|
| | | 3 | 7 | 11 | 15 | 19 | 23 | 27 | 31 |
| 0.50 | 1.044 | 0.711 | 0.818 | 0.866 | 0.893 | 0.911 | 0.925 | 0.935 | 0.943 |
| | | 0.847 | 0.914 | 0.942 | 0.958 | 0.968 | 0.975 | 0.981 | 0.986 |
| | | 1.153 | 1.130 | 1.117 | 1.109 | 1.103 | 1.099 | 1.095 | 1.092 |
| | | 1.179 | 1.161 | 1.148 | 1.138 | 1.131 | 1.126 | 1.121 | 1.117 |
| 0.60 | 1.019 | 0.756 | 0.839 | 0.876 | 0.898 | 0.913 | 0.923 | 0.931 | 0.937 |
| | | 0.861 | 0.915 | 0.937 | 0.949 | 0.958 | 0.963 | 0.968 | 0.972 |
| | | 1.107 | 1.088 | 1.078 | 1.071 | 1.066 | 1.063 | 1.060 | 1.058 |
| | | 1.128 | 1.113 | 1.102 | 1.095 | 1.089 | 1.084 | 1.081 | 1.078 |
| 0.70 | 1.004 | 0.810 | 0.870 | 0.897 | 0.913 | 0.924 | 0.932 | 0.938 | 0.943 |
| | | 0.886 | 0.926 | 0.942 | 0.952 | 0.958 | 0.962 | 0.966 | 0.968 |
| | | 1.071 | 1.056 | 1.049 | 1.044 | 1.040 | 1.037 | 1.035 | 1.033 |
| | | 1.087 | 1.075 | 1.067 | 1.062 | 1.057 | 1.054 | 1.051 | 1.048 |
| 0.75 | 1.000 | 0.839 | 0.888 | 0.911 | 0.924 | 0.933 | 0.940 | 0.944 | 0.948 |
| | | 0.902 | 0.935 | 0.948 | 0.956 | 0.961 | 0.965 | 0.967 | 0.970 |
| | | 1.056 | 1.044 | 1.037 | 1.033 | 1.030 | 1.027 | 1.026 | 1.024 |
| | | 1.069 | 1.060 | 1.053 | 1.048 | 1.044 | 1.041 | 1.039 | 1.037 |
| 0.80 | 0.997 | 0.869 | 0.908 | 0.926 | 0.937 | 0.944 | 0.949 | 0.953 | 0.956 |
| | | 0.919 | 0.945 | 0.956 | 0.962 | 0.966 | 0.969 | 0.971 | 0.973 |
| | | 1.042 | 1.032 | 1.027 | 1.024 | 1.021 | 1.019 | 1.018 | 1.017 |
| | | 1.053 | 1.045 | 1.040 | 1.036 | 1.033 | 1.030 | 1.028 | 1.027 |
| 0.85 | 0.996 | 0.901 | 0.929 | 0.943 | 0.951 | 0.956 | 0.960 | 0.963 | 0.965 |
| | | 0.937 | 0.957 | 0.965 | 0.969 | 0.972 | 0.975 | 0.976 | 0.978 |
| | | 1.030 | 1.022 | 1.018 | 1.016 | 1.014 | 1.013 | 1.012 | 1.011 |
| | | 1.038 | 1.032 | 1.028 | 1.025 | 1.023 | 1.021 | 1.020 | 1.018 |
| 0.90 | 0.996 | 0.933 | 0.952 | 0.961 | 0.966 | 0.969 | 0.972 | 0.974 | 0.975 |
| | | 0.957 | 0.970 | 0.975 | 0.978 | 0.980 | 0.982 | 0.983 | 0.984 |
| | | 1.019 | 1.014 | 1.011 | 1.009 | 1.008 | 1.007 | 1.007 | 1.006 |
| | | 1.024 | 1.020 | 1.018 | 1.016 | 1.014 | 1.013 | 1.012 | 1.011 |
| 1.25 | 1.027 | 0.952 | 0.963 | 0.970 | 0.975 | 0.979 | 0.983 | 0.985 | 0.987 |
| | | 1.122 | 1.091 | 1.078 | 1.071 | 1.066 | 1.062 | 1.059 | 1.057 |
| | | 0.967 | 0.980 | 0.987 | 0.992 | 0.995 | 0.998 | 1.000 | 1.001 |
| | | 1.178 | 1.134 | 1.114 | 1.101 | 1.093 | 1.087 | 1.082 | 1.078 |
| 1.50 | 1.071 | 0.916 | 0.939 | 0.955 | 0.966 | 0.974 | 0.981 | 0.986 | 0.991 |
| | | 1.259 | 1.199 | 1.173 | 1.158 | 1.149 | 1.141 | 1.136 | 1.131 |
| | | 0.948 | 0.976 | 0.990 | 1.000 | 1.007 | 1.012 | 1.016 | 1.019 |
| | | 1.365 | 1.282 | 1.242 | 1.218 | 1.202 | 1.190 | 1.180 | 1.173 |
| 1.75 | 1.127 | 0.890 | 0.925 | 0.950 | 0.967 | 0.980 | 0.990 | 0.999 | 1.006 |
| | | 1.404 | 1.317 | 1.280 | 1.258 | 1.243 | 1.232 | 1.224 | 1.218 |
| | | 0.939 | 0.982 | 1.005 | 1.020 | 1.030 | 1.037 | 1.044 | 1.049 |
| | | 1.558 | 1.438 | 1.380 | 1.345 | 1.321 | 1.304 | 1.290 | 1.279 |

Table 5: Percentage points for median of 7 points, power product with error in the identification of the axes; $h_1(\Theta_B, \Theta_A) = \Theta_A^{0.75}\Theta_B^{0.25}$

| $r_0$ | Percentage Points<br>5%, | <br>50% | <br>95% |
|---|---|---|---|
| 0.50 | 0.996 | 1.402 | 1.626 |
| 0.70 | 0.949 | 1.160 | 1.277 |
| 0.90 | 0.973 | 1.037 | 1.073 |
| 1.25 | 0.867 | 0.949 | 1.091 |
| 1.50 | 0.778 | 0.936 | 1.204 |
| 1.75 | 0.717 | 0.946 | 1.330 |

Table 6: Percentage points for median of 7 points, $h_1(\Theta_A, \Theta_B) = \Theta_A^{0.5}\Theta_B^{0.5}$

| $r_0$ | Percentage Points<br>5%, | <br>50% | <br>95% |
|---|---|---|---|
| 0.50 | 0.903 | 1.210 | 1.374 |
| 0.70 | 0.908 | 1.079 | 1.172 |
| 0.90 | 0.963 | 1.016 | 1.046 |
| 1.25 | 0.913 | 0.987 | 1.113 |
| 1.50 | 0.855 | 1.001 | 1.243 |
| 1.75 | 0.814 | 1.033 | 1.384 |

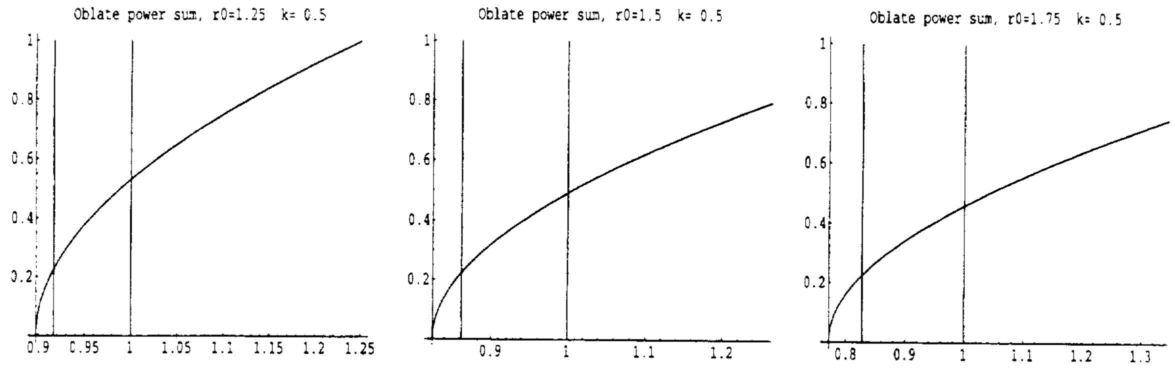

Figure 12: Cumulative distributions of the ratio of the measured value of $H_0$ to the true value for oblate spheroids using the estimator $h_1(\Theta_A, \Theta_B) = [(\Theta_A^{0.5} + \Theta_B^{0.5})/2]^2$. The 5% to 95% confidence interval for the median of 7 data points is indicated.

Table 7: Percentage points for median of 7 points, $h_1(\Theta_A, \Theta_B) = \left[\left(\Theta_A^{0.5} + \Theta_B^{0.5}\right)/2\right]^2$

| $r_0$ | Percentage Points | | |
|---|---|---|---|
| | 5% | 50% | 95% |
| 0.50 | 0.911 | 1.237 | 1.413 |
| 0.70 | 0.910 | 1.085 | 1.181 |
| 0.90 | 0.963 | 1.017 | 1.047 |
| 1.25 | 0.916 | 0.989 | 1.113 |
| 1.50 | 0.862 | 1.006 | 1.244 |
| 1.75 | 0.828 | 1.041 | 1.386 |

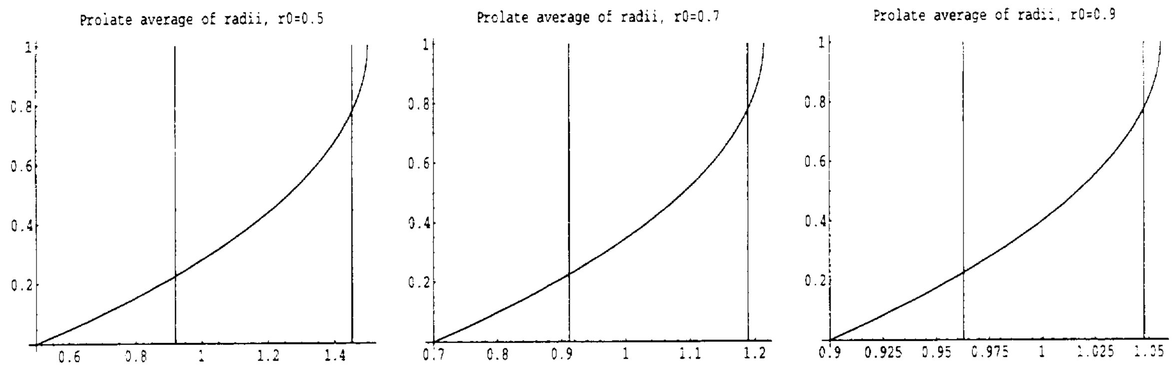

Figure 13: Cumulative distributions of the ratio of the measured value of $H_0$ to the true value for prolate spheroids using the estimator $h_1(\Theta_A, \Theta_B) = (\Theta_A + \Theta_B)/2$. The 5% to 95% confidence interval for the median of 7 data points is indicated.

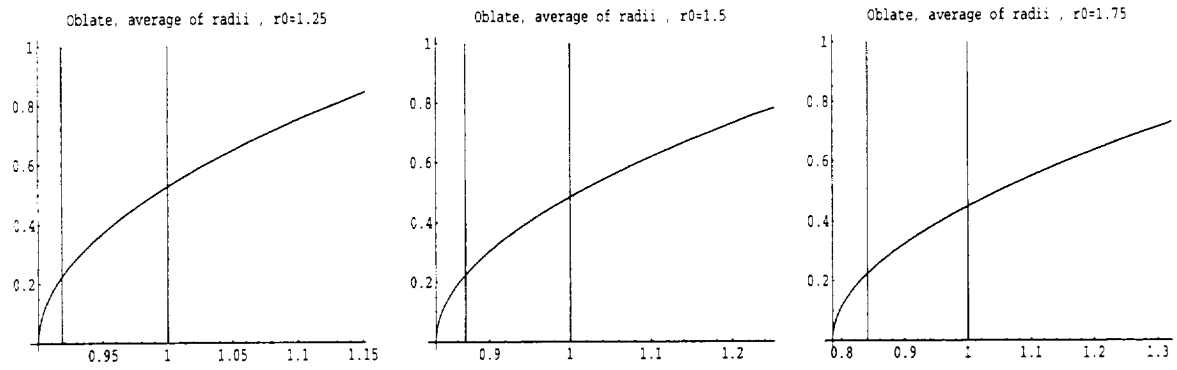

Figure 14: Cumulative distributions of the ratio of the measured value of $H_0$ to the true value for oblate spheroids using the estimator $h_1(\Theta_A, \Theta_B) = (\Theta_A + \Theta_B)/2$. The 5% to 95% confidence interval for the median of 7 data points is indicated.

Table 8: Percentage points for median of 7 points, $h_1(\Theta_A, \Theta_B) = (\Theta_A + \Theta_B)/2$

| $r_0$ | Percentage Points | | |
|---|---|---|---|
| | 5%, | 50% | 95% |
| 0.50 | 0.920 | 1.263 | 1.452 |
| 0.70 | 0.912 | 1.090 | 1.189 |
| 0.90 | 0.963 | 1.017 | 1.048 |
| 1.25 | 0.918 | 0.990 | 1.113 |
| 1.50 | 0.870 | 1.010 | 1.245 |
| 1.75 | 0.841 | 1.049 | 1.388 |